The Role of Momentum Fluxes in Shaping the Life Cycle of a Baroclinic Wave

G. BALASUBRAMANIAN

Atmospheric and Oceanic Sciences Program, Princeton University, Princeton, New Jersey

STEPHEN T. GARNER

Geophysical Fluid Dynamics Laboratory/NOAA, Princeton, New Jersey

(Manuscript received 28 August 1995, in final form 12 August 1996)

ABSTRACT

The wide disparities in baroclinic wave development between spherical and Cartesian geometry are investigated with the purpose of assessing the role of the eddy momentum fluxes. Differences are already significant at the linear stage, as momentum fluxes are predominantly poleward in spherical geometry and predominantly equatorward in Cartesian geometry. More important, the low-level flux convergence is displaced poleward on the sphere and equatorward on the plane. On the sphere, these circumstances lead to rapid poleward movement of the low-level zonal-mean jet. The anticyclonic horizontal shear region expands as the jet feeds back on the momentum flux. The wave breaks anticyclonically and quickly zonalizes. In the Cartesian life cycle, the equatorward displacement of the flux convergence is counteracted by the mean meridional circulation and there is consequently a weaker feedback with the horizontal shear. The wave breaks, in this case cyclonically, but then takes much longer to zonalize. On the sphere, the angular velocity gradient in uniform westerly or easterly flow adds a separate mechanism for converting eddy kinetic energy to zonal mean, further hastening the zonalization process.

It is possible to change the sign of the eddy momentum flux and the sense of the breaking in either geometry by slightly changing the basic flow. For example, cyclonic roll-up on the sphere can be obtained by adding weak cyclonic barotropic shear, as highlighted in a recently published study. Similarly, the addition of anticyclonic barotropic shear in a Cartesian simulation leads to anticyclonic wave breaking. An easterly jet on the sphere allows cyclonic breaking, but the wave still zonalizes rapidly, as in the case of a westerly jet. The persistence of the nonlinear eddies in these diverse experiments is not well correlated with the minimum value of the refractive index for Rossby waves, as suggested in the referenced study. It is proposed that the longevity of residual vortices after wave breaking is determined not by the sign of the vorticity or the breadth of the waveguide, but by the sign of the momentum flux and the geometry of the model.

1. Introduction

In order to characterize the interaction between mean flow and baroclinic eddies, most studies have focused on the finite-amplitude development of normal modes in a zonally symmetric baroclinic jet. Such waves grow exponentially at all altitudes for a few days depending on the initial amplitude and then progressively enter a nonlinear stage from the bottom up. Nonlinearity eventually stops the growth of the wave. This equilibration process[1] can often be characterized as strongly cyclonic or strongly anticyclonic, according to the predominant meridional tilt of the wave prior to equilibration or the sign of the vorticity between the two main barotropic zonal-mean jets that are created. Snyder et al. (1991), Nakamura (1993), and Rotunno et al. (1994) have discussed the tendency of baroclinic waves in Cartesian models to exhibit cyclonic (SE–NW) tilt. Observations (Starr 1968; Peixoto and Oort 1984) and modeling studies on the sphere (Hollingsworth 1976; Simmons and Hoskins 1978) have documented predominantly poleward momentum fluxes, associated with anticyclonic (SW–NE) tilt. In this study, we analyze the differences, due to model geometry, between the two extreme types of equilibration.

Differences due to geometry have never been investigated systematically using multilevel models. While the solutions in both Cartesian and spherical geometry exhibit common features like lower- and upper-level frontogenesis, occlusion, and wave breaking, there are major differences in morphology, starting with the aforementioned meridional eddy tilt, that significantly

[1] Since ''wave breaking'' is commonly understood to imply turbulent energy transfer to smaller and larger scales, we use ''equilibration'' to refer to a terminal process that may or may not involve such a cascade.

Corresponding author address: Dr. G. Balasubramanian, Lawrence Livermore National Laboratory, Atmospheric Science Division, P.O.Box 808, L-262, Livermore, CA 94551-9900.

impact the mean flow. Studies of baroclinic life cycles on the sphere include Simmons and Hoskins (1976, 1977, 1978, 1980), Thorncroft et al. (1993), and Hines and Mechoso (1993). Cartesian modeling studies include Mudrick (1974), Hoskins and West (1979), Takayabu (1986), Polavarapu and Peltier (1990), Snyder et al. (1991), Davis et al. (1991), and Rotunno et al. (1994). All of these, like the present study, consider modal waves in zonally symmetric basic flows. The relevance of normal modes and zonal symmetry in realistic, turbulent climate systems is a matter of some controversy (e.g., Farrell 1989; Branstator 1995; Whitaker and Dole 1995). Here we only wish to use the normal-mode framework to understand dynamical processes that are exclusively associated with model geometry.

Whitaker and Snyder (1993, hereafter WS) recently compared nonlinear baroclinic development in spherical and Cartesian geometry using a two-layer isentropic-coordinate model. They discounted the differences between the normal modes and emphasized those that appear at finite amplitude. In particular, they showed that the meridional displacement of cyclones and anticyclones tended to strengthen the anticyclones and weaken the cyclones on the sphere. Through scale analysis and barotropic vorticity inversion, they determined that the dominant spherical ''metric'' effect underlying this asymmetry is the one associated with variations in the length, rather than the curvature, of the latitude circles. There is no corresponding effect in Cartesian geometry, where the cyclones and anticyclones therefore tend to be stronger and weaker, respectively, than on the sphere. Since vorticity is not generally conserved in a baroclinic model, WS applied their argument to a stage of nonlinear development when vortices are highly barotropic or equivalent barotropic. In their numerical solutions, anticyclonic wrapping of potential vorticity (PV) in the upper layer in spherical geometry and cyclonic wrapping in Cartesian geometry were noted.

The meridional displacement of highs and lows is associated with the creation of zonal-mean winds. At early times, this is accomplished primarily by the mean meridional circulation. As stipulated by WS, the tendency to favor anticyclones and anticyclonic mean shear on the sphere as this process goes forward does not entirely control the outcome of the wave development. Simmons and Hoskins (1980) and Thorncroft et al. (1993, hereafter THM) demonstrated an overriding effect due to small differences in zonal-mean initial conditions. In THM's control experiment (''LC1''), the tropospheric jet is symmetric and normal-mode wave breaking is anticyclonic. However, by adding a weak, cyclonic, barotropic shear across the jet, they obtained cyclonic breaking (''LC2'') without removing the spherical effect mentioned by WS.

In looking for a more robust mechanism to explain the high sensitivity to geometry and initial conditions, we will consider the direct role of low-level momentum fluxes. The predominant direction of the flux is determined by the meridional tilt of the eddy long before it can be considered equivalent barotropic and vorticity conserving. Unlike the mean meridional circulation that displaces the pressure centers toward pole and equator at early times, momentum fluxes tend to become involved in a positive feedback with the zonal-mean wind. Therefore, they are predisposed to become a dominant mechanism in wave equilibration. Although the development of mean meridional shear by eddy momentum fluxes tends to accentuate eddy gyres with the same-sign vorticity, THM's solutions show that the meridional tilt of a gyre is not uniquely determined by the sign of its vorticity: both cyclones and anticyclones may be tilted SW–NE (''anticyclonically'') or SE–NW (''cyclonically''). For these reasons, we concentrate on eddy tilt rather than eddy vorticity (or streamfunction) in trying to understand different types of wave breaking.

Since the momentum fluxes in normal modes tend to be upgradient (McIntyre 1970; Held and Andrews 1983; James 1987; Nakamura 1993), there is an early positive feedback between zonal-mean acceleration and barotropic decay of eddies due to momentum fluxes in the region of baroclinic conversion. James (1987) showed that barotropic shear hinders the optimal, modal growth of baroclinic disturbances by reducing their meridional coherence, the effect referred to as the ''barotropic governor.'' According to Nakamura (1993), positive feedback in the barotropic governor allows the shape of the linear wave to determine the nature of the nonlinear equilibration. He notes that normal-mode momentum fluxes are very sensitive to small asymmetries in either the physical model (beta, sphericity, nongeostrophy) or the zonal-mean flow (cyclonic or anticyclonic barotropic shear). As a result, geometry and mean flow asymmetries can exert a greater influence on equilibration through momentum fluxes than through heat fluxes. One of the most elegant tools for understanding wave–mean-flow interaction is the Eliassen–Palm (EP) flux (e.g., Edmon et al. 1980). Unfortunately, analysis of EP flux divergence in the context of transformed zonal-mean equations automatically ignores the distinction between heat flux and momentum flux. The former is part of the equilibration process but does not directly involve a positive feedback.

THM found that changing initial conditions to reverse the sign of the equilibration also drastically alters the longevity of the residual vortices. To explain this difference in eddy longevity, they compared upper-level zonal-mean flow conditions using EP flux and refractive-index diagnostics. They suggested that the case of cyclonic equilibration (LC2) develops long-lived coherent vortices partly because a ''refractive index barrier'' prevents the propagation of wave activity to the subtropical critical latitudes via upper levels. Freer meridional propagation was believed to allow rapid zonalization of the wave in the anticylonic control case (LC1). We will argue that poorer cooperation between the meridional circulation and the low-level momentum-

flux convergence is mainly responsible for the slower zonalization in LC2. Stronger barotropic decay and the runaway expansion of the zonal-mean shear zone in LC1 prevent the eddies in that case from becoming organized into coherent structures. A similar argument will be used for the Cartesian–spherical contrast. Also, the barotropic decay on the sphere is strengthened by a spherical metric term that favors eddy decay when momentum fluxes are poleward across mean westerlies.

The organization of the paper is as follows. In section 2, we briefly describe the models and the initial conditions used for the Cartesian and spherical simulations. The synoptic features of the waves, the eddy momentum fluxes, the migration of the low-level jet in response to the momentum fluxes, and the barotropic decay process are discussed in section 3. A brief discussion of anomalous cases (due to barotropic shear or reversed jets) is given in section 4. One of these cases suggests that a weak barotropic governor may be necessary but is not sufficient for long-lived vortices. Section 5 contains the concluding remarks.

2. The models

For the spherical simulations, we use a standard hydrostatic, sigma-coordinate, spectral-transform model of the type described by Held and Suarez (1994), Bourke (1974), and Hoskins and Simmons (1975). Aliasing due to quadratic products is removed. There are 20 equally spaced levels in the vertical, with the top of the model at zero pressure. A leapfrog scheme, including the time filter described by Robert (1966), is used for time stepping. The truncation is triangular and we conduct all integrations with the resolution T95. The model is dry and frictionless except for some internal ∇^2 diffusion added to the vorticity, divergence, and temperature tendency equations. The diffusion coefficient is chosen to give a decay rate of $(3\ \mathrm{h})^{-1}$ for the shortest retained scale.

For the Cartesian simulation, we use the gridpoint model described in Balasubramanian and Yau (1994). It is a standard hydrostatic, pressure-coordinate gridpoint model, employing a Charney–Phillips grid in the vertical. For this model also, we use 20 equally spaced vertical levels, with the top of the model at zero pressure. The domain length in the zonal direction is taken to be equal to the wavelength of wavenumber 6 at 45° on the sphere. Periodicity is assumed in this direction. The model has a channel geometry with vertical walls near the equator and pole. The artificial walls are located far enough away from the evolving waves to avoid contamination during the standard integration period of 10 days. Following WS, the full variation of the Coriolis parameter with latitude is included so that the difference in the evolution of the waves in the two models is entirely due to metric effects. A grid length of 111 km is used both in the x and y directions. A diffusion coefficient of $1.15 \times 10^5\ \mathrm{m^2\ s^{-1}}$, corresponding to a decay rate of $(3\mathrm{h})^{-1}$ for the $2\Delta x$ wave, is used in the Cartesian model.

Although the spherical and Cartesian models use spectral and finite-difference methods, respectively, and use different forms of the equations of motion (vorticity–divergence in the spherical model and momentum in the Cartesian model), the similarity of the wave evolutions to those of past studies (Takayabu 1986; Polavarapu and Peltier 1990; Hines and Mechoso 1993; THM) suggests that the solutions are not sensitive to the numerical methods.

Initial conditions

Both the spherical model (SM) and Cartesian model (CM) are initialized with a zonally symmetric jet plus the fastest-growing normal mode for the given zonal scale. The jet is centered at 45° on the sphere. The wave is given an initial amplitude of $1\ \mathrm{m\ s^{-1}}$ for the meridional velocity at the lower boundary. For the spherical simulation, we use the basic state shown in Fig. 1a. In the troposphere, the wind and thermal fields are essentially those of THM for their simulation LC1. The structure of the jet is given by

$$u = u_0 F(p)\sin^3[\pi(\sin^2\phi)]. \tag{1}$$

The maximum speed, $47\ \mathrm{m\ s^{-1}}$, occurs at $\phi = 45°$ and $p = 175$ mb. Since we have used 20 equally spaced sigma levels, the tropopause and the stratosphere are not well represented. The diffuse tropopause somewhat weakens the baroclinic instability, especially at high latitudes where the planetary vorticity gradient is small. Note that the stratosphere and upper boundary are barotropic (unlike THM's upper atmosphere), which further weakens the linear instability.

The two-dimensional PV field from the spherical model is inverted in Cartesian geometry using thermal-wind balance, and the resulting wind and mass fields are used as the initial condition for the Cartesian simulation (Fig. 1b). The PV field of this basic state is shown in Fig. 2. The initial geopotential field from the spherical model is imposed at all boundaries for the PV inversion, thereby matching the potential temperature at channel walls and (approximately) the zonal wind at horizontal boundaries. The geostrophic relation in the Cartesian model is

$$fu = -\frac{\partial\Phi}{\partial y}, \tag{2}$$

while in the spherical model it is

$$\left(f + \frac{u\tan\phi}{a}\right)u = -\frac{1}{a}\frac{\partial\Phi}{\partial\phi}. \tag{3}$$

The maximum jet velocity in the spherical model is slightly smaller than that in the Cartesian model because of the curvature term on the left side of (3). The basic-state vorticity in SM is given by

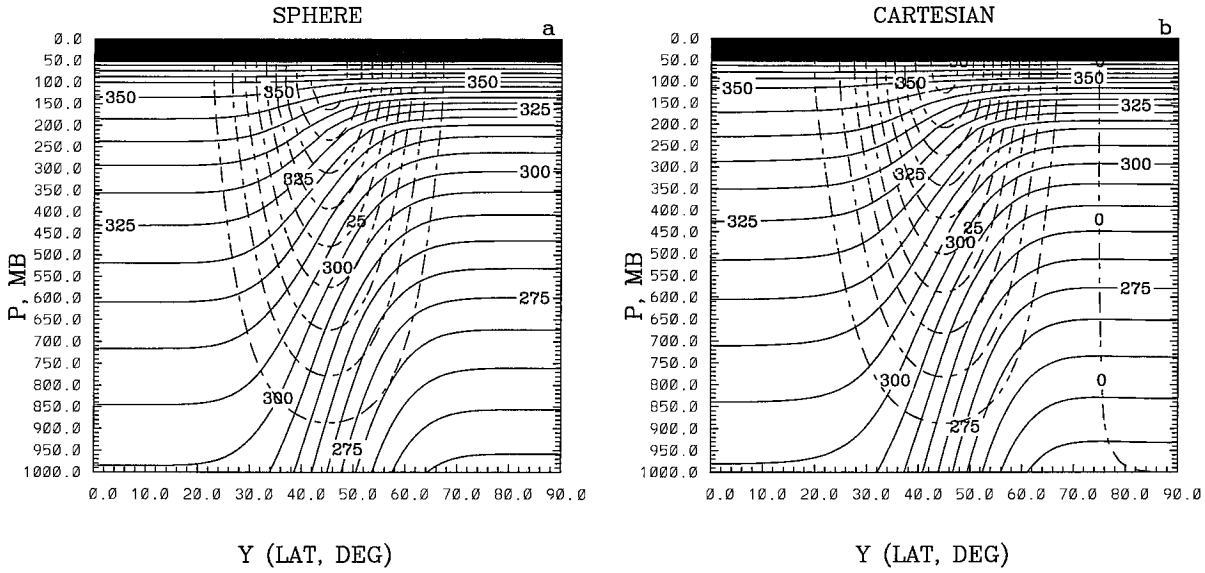

FIG. 1. Basic-state potential temperature (solid lines, every 5 K) and zonal wind (dashed, every 5 m s^{-1}) in the (a) spherical and (b) Cartesian geometries.

$$\zeta = -\frac{\partial u}{a\partial\phi} + \frac{u\tan\phi}{a}. \tag{4}$$

The cyclonic shear on the poleward side of the jet maximum is slightly diminished, and the anticyclonic shear augmented in SM because of the second term in (4), associated with the curvature of the latitude circles.

We also conducted some experiments with the same wind profile in the Cartesian model as in the spherical model. The resulting small differences in PV distribution had no important effect on the baroclinic wave development.

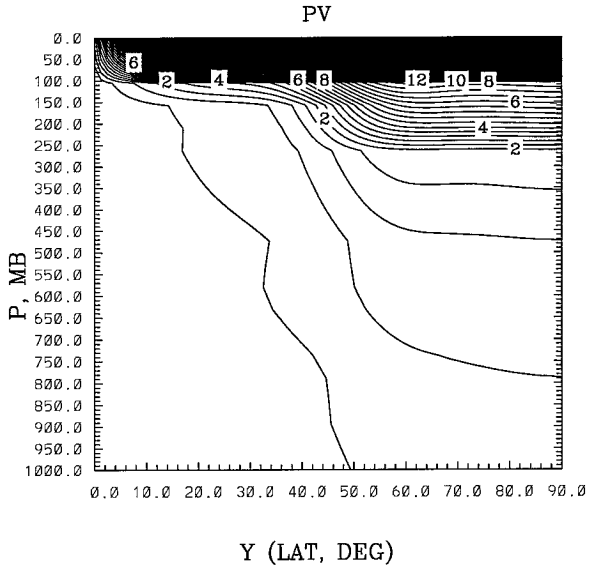

FIG. 2. Meridional cross section of the PV distribution used in both the spherical and Cartesian geometry. The contour interval is 0.4 PVU (PVU = 10^{-6} K m^2 s^{-1} kg^{-1}).

3. Results

a. Normal modes

In order to compare with THM and WS, we study wavenumber 6. On the sphere, this mode has a growth rate of 0.71 day^{-1} and a phase speed of 12° day^{-1}. In the Cartesian model, the same wavelength has a growth rate of 0.68 day^{-1} and a phase speed of 16° day^{-1}. These are the results of long-term numerical integrations in which the nonlinearity was kept small by renormalizing the wave amplitude. The meridional component of velocity at 975 and 325 mb is plotted for the normal modes in Fig. 3. Both the Cartesian and spherical modes have a westward tilt of about 12° between 975 and 325 mb. They also tilt northward with height in both geometries. A related poleward shift of the upper-level eddy kinetic energy (EKE) maximum was noted by THM. Snyder et al. (1991) observed that the tilt is along sloping absolute momentum surfaces, as predicted by semigeostrophic theory.

As we will see in section 3b, the modes also have a strong tilt on horizontal surfaces. In their quasigeostrophic (QG) study, Held and Andrews (1983) found that barotropic eddy momentum flux is upgradient when the jet width is greater than the Rossby radius of deformation. This is consistent with the present solutions, in which the horizontal tilt tends to be with the basic shear, changing sign near the jet axis. However, we notice an overall bias in the tilt that depends on the model geometry. The spherical modes (Fig. 3a) are weakly biased NE–SW (anticyclonically) and the Cartesian modes (Fig. 3b) are biased NW–SE (cyclonically). The associated momentum fluxes, plotted in Fig. 4, show a poleward (equatorward) directional bias and slight

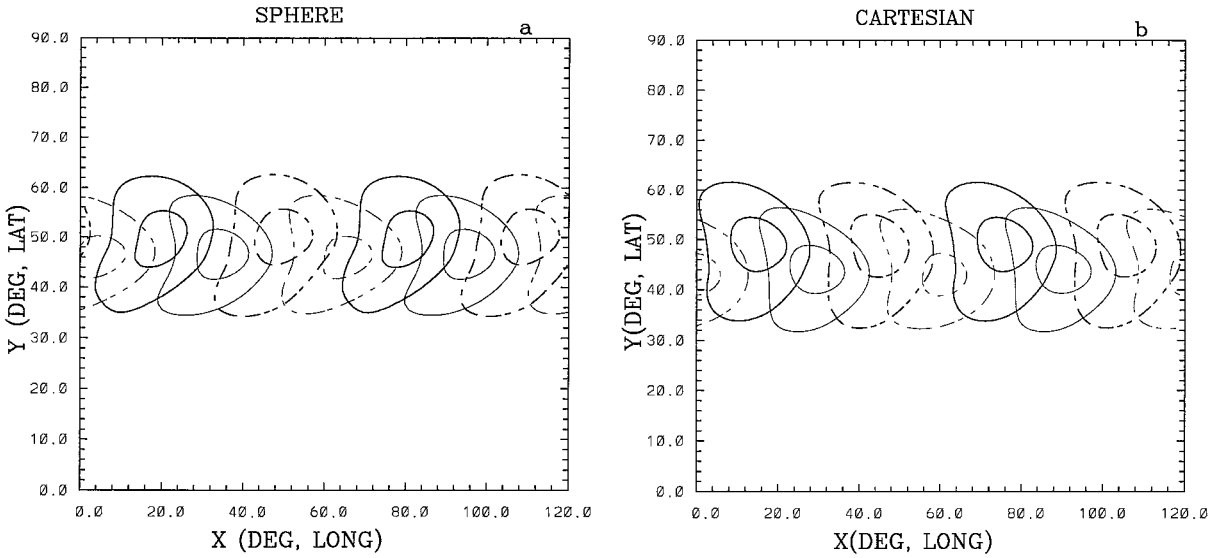

FIG. 3. Meridional velocity of the normal mode at 975 mb (thin lines) and at 325 mb (thick lines) for the (a) spherical and (b) Cartesian geometries. The contour interval is 0.5 m s^{-1}.

poleward (equatorward) shift in the convergence in SM (CM).

Snyder et al. (1991) traced the NW–SE bias of the Cartesian modes to the ageostrophic vorticity induced by curvature in the total flow. In the present solutions, an additional bias arises from the tilt of the mode along absolute momentum surfaces. Since the low-level wind is calm, this allows the modes to be dominated by the cyclonic shear at upper levels. We assume a tendency to tilt with the horizontal shear, which is consistent with an argument by Davies et al. (1991) for growing baroclinic waves.[2] On the sphere, the sources of cyclonic bias are evidently slightly weaker than countervailing tendencies toward anticyclonic tilt. We speculate that the variation in the length of latitude circles produces the anticyclonic bias in spherical normal modes through the resulting variation in the local Rossby wave phase speed. As implied by James (1987), a normal mode must possess compensation for any tendency for phase speed to vary across the mode. In the present example, an increase in vertical tilt on the poleward side of the jet provides the right compensation and also the anticyclonic tilt.

b. Synoptic features

In this section, we briefly discuss the major synoptic features of the CM and SM solutions. The label ''C'' in the figures identifies the center of the surface cyclone.

1) LOW-LEVEL CYCLONE EVOLUTION

The geopotential deviation from the initial basic state at 975 mb on days 3, 5, 7, and 9 is presented for CM and SM in Figs. 5 and 6, respectively. Figure 6 is essentially the same as the LC1 case of THM, shown in their Fig. 6. The major difference between CM and SM on day 3 is the meridional tilt. The eddy in CM shows predominantly cyclonic tilt (Fig. 5a), while the spherical mode is more symmetric (Fig. 6a). The cyclones have migrated from 45° latitude to 49° and 50° in CM and SM, respectively. By day 5, the overall bias toward NE–SW tilt in the SM wave has become quite noticeable again (Fig. 6b), as the cyclones have lost most of their meridional tilt. As noted by Snyder et al. (1991), the cyclonic geopotential anomaly is stronger than the anticyclonic anomaly because of the gradient wind effect and not because of nonlinear vortex stretching.

On day 7, the wave in SM (Fig. 6c) shows further anticyclonic tilt. The zonal extension of the closed circulations reflects the growth of the zonal-mean wind at the expense of the eddy. As we will see in section 3c, the eddy kinetic energy in SM has peaked at this time, but the wave in CM is still growing. On day 9, the SM eddy is essentially destroyed, most of its energy having been converted to zonal-mean flow (Fig. 6d). In sharp contrast, a cyclonic roll-up has occurred in CM. The nearly isotropic vortices in this solution resemble those of the cyclonic life cycle LC2 simulated by THM on the sphere. THM emphasized the remarkable longevity of these rolled-up lows.

2) LOW-LEVEL TEMPERATURE EVOLUTION

The low-level (975-mb) temperature fields on day 5 and 7 for the two models can be compared in Fig. 7.

[2] These authors stop short of explaining the *sign* of the meridional tilt. Since the observed meridional tilt is barotropically damping, the explanation is likely to be found in the constraints on meridional variations of *vertical* tilt necessary to ensure baroclinic instability.

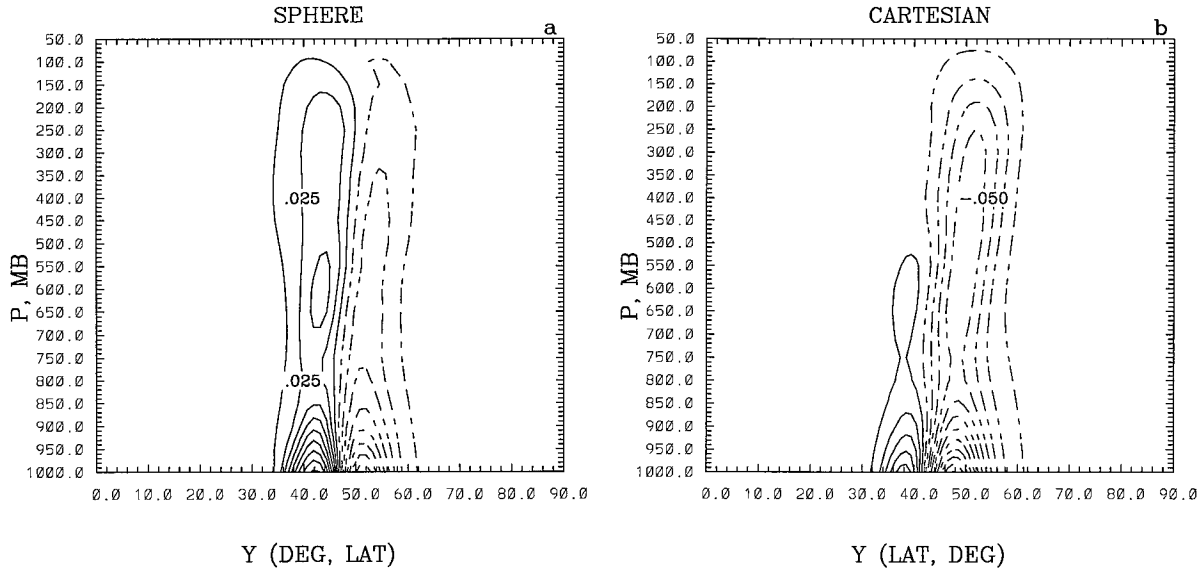

FIG. 4. Horizontal eddy momentum fluxes (every 0.015 m^2 s^{-2}) in the normal modes in (a) spherical and (b) Cartesian geometry.

Despite strong similarities at day 5, especially in the frontal zones, the stronger SW–NE orientation of the wave in SM is clearly discernible (Figs. 7a,c). Interestingly, the thermal gradient across the warm front in CM is weaker than in SM. By day 7 (Figs. 7b,d), the waves have evolved to the stage of ''seclusion,'' with a warm pool of air cut off near the cyclone center (Polavarapu and Peltier 1990; Davies et al. 1991; THM). The warm front in CM (Fig. 7c) has wrapped to the west around the cyclone center to form the so-called bent-back warm front (Shapiro and Keyser 1990). Near this front, the isotherms are arc shaped. In SM, the isotherms near the warm front are more sheared out in the zonal direction, a consequence of the strong poleward momentum fluxes and the barotropic eddy decay to be shown in section 3c.

Rotunno et al. (1994) showed that the cyclonic (SE–NW) tilt of the CM mode leads to early development of the warm front compared to the corresponding semigeostrophic model. However, we find similar early warm frontogenesis in the more anticyclonic SM solution as well. Davies et al. (1991) noted that ambient cyclonic shear in a semigeostrophic model enhances the warm thermal anomaly, while ambient anticyclonic shear enhances the cold thermal anomaly at the surface. The secluded air in the relatively cyclonic CM solution is warmer than that in SM by about 6 K, in agreement with Davies et al., but there are no important differences in the strength of the cold anomalies.

3) UPPER-LEVEL PV EVOLUTION

In Figs. 8 and 9, we have plotted the evolution of PV on the $\theta = 320$ K surface for CM and SM, respectively. The $\theta = 320$ K surface is at about 500 mb in the Tropics and about 200 mb in the polar regions. One can see from the location of the isentropic PV gradient that this particular potential temperature surface crosses the tropopause on the cyclonic side of the jet. The upper-level maps for CM and SM resemble the life cycles LC2 (cyclonic) and LC1 (anticyclonic), respectively, described in THM and Davies et al. (1991). The general SE–NW bias in CM and the SW–NE bias in SM in the upper levels are apparent on day 3. Only the northernmost contours in CM and southernmost contours in SM show the reversed tilt. These differences between CM and SM are amplified by day 5 (Figs. 8b and 9b).

By day 7, the upper-level waves are fully developed and sharp gradients of PV are seen. The PV contours in CM (Fig. 8c) suggest predominantly a cyclonic roll-up. Any cyclonic wrapping on the sphere is strongly dominated by the shearing effect of the anticyclonic zonal-mean wind (Fig. 8c), as originally noted by THM. This is consistent with the strong poleward eddy momentum fluxes at upper levels in SM (cf. Fig. 15c in section 3d). After the wave has zonalized in SM on day 9 (Fig. 9d), cyclonic roll-up continues in CM and strong PV gradients persist around the edges of the vortex. These gradients are sharp enough to generate some gridpoint noise in the model. There is relatively little sign of barotropic decay in CM.

Both CM and SM undergo an occlusion process in which upper and lower streamfunction and PV anomalies become aligned. As we will see, this process is not necessarily the primary reason for the wave equilibration. However, there is an interesting synoptic difference between CM and SM in this connection. In the spherical solution, the anticyclonic part of the eddy is less elongated meridionally and becomes better aligned in the vertical. The cyclonic part moves to the poleward side of the anticyclones at low levels and to the equa-

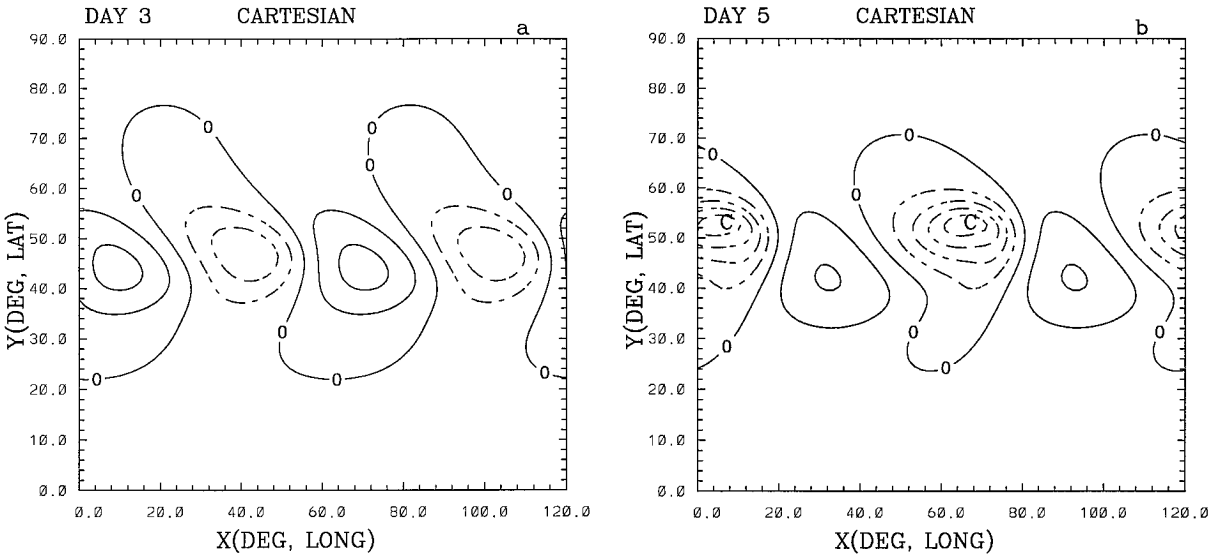

FIG. 5. Evolution of the low-level cyclone in Cartesian geometry. The geopotential deviation from the basic state at 975 mb on days (a) 3, (b) 5, (c) 7, and (d) 9. The contour interval for (a) is 2 dm and for (b), (c), and (d) is 5 dm.

torward side at upper levels. This implies that the anticyclonic part of the perturbation becomes more barotropic than the cyclonic part. The reverse is true in SM, where cyclones are more barotropic and isotropic than anticyclones. As we will see in section 3d, these differences are directly related to the different ways in which the zonal-mean jets are modified during nonlinear development.

c. Time series

In Fig. 10, we have plotted the minimum geopotential anomaly and maximum relative vorticity anomaly at 975 mb as a function of time for SM and CM. The two simulations produce cyclones of similar intensity until 5.5 days. Thereafter, the SM cyclones deepen more slowly than their CM counterparts. The two-layer model of WS produces a much stronger circulation around the low centers in Cartesian geometry than in spherical geometry by day 5 (their Fig. 4). Our computation of streamfunction anomaly for day 5 (not shown) is consistent with this difference as far as sign, but our CM lows are only about 10% stronger by this measure.

More striking than the effect of geometry on geopotential or streamfunction anomaly is its effect on domain-averaged eddy kinetic energy:

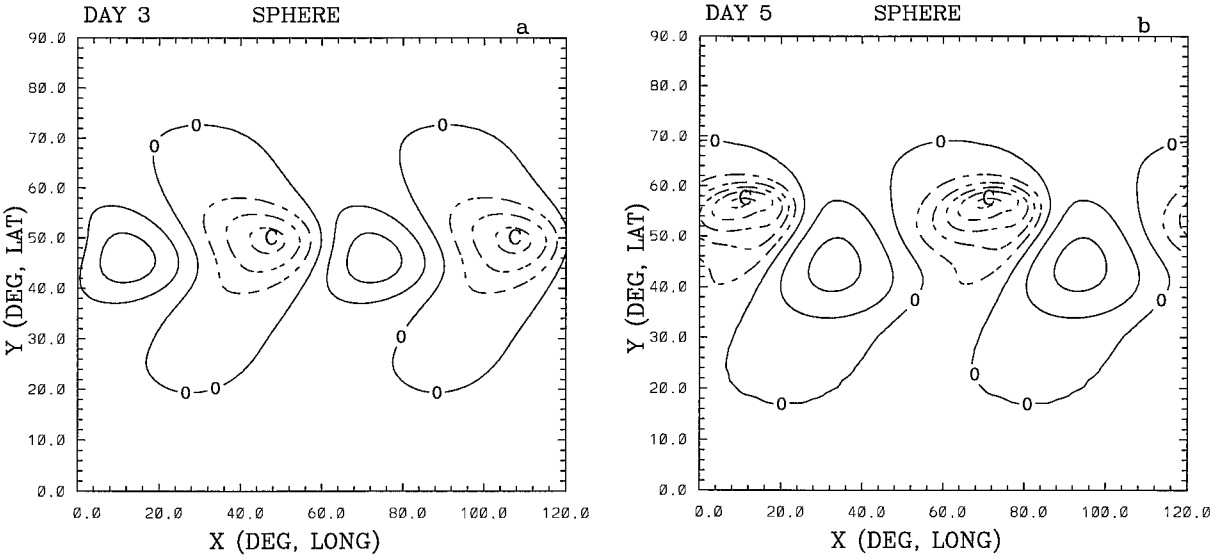

FIG. 6. Same as in Fig. 5 except for spherical geometry.

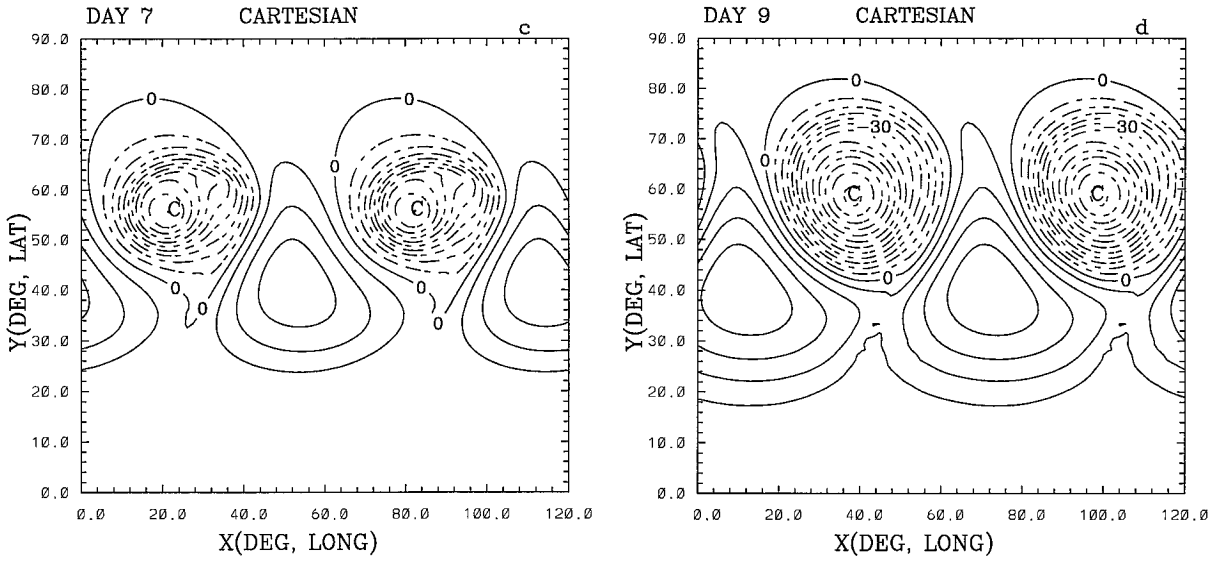

FIG. 5. (*Continued*)

$$\langle K_E \rangle = \int_0^{p_0} \{K_E\}\, dp, \tag{5}$$

where $K_E \equiv 2^{-1}(u'^2 + v'^2)$. Here the prime denotes a departure from the zonal mean, and the curly brackets denote an average over a pressure surface. The time series of $\langle K_E \rangle$ are shown in Fig. 11. In SM, the EKE decreases sharply after day 7, while in CM the decay starts on day 9 and then takes longer. Thus, despite similar linear growth rates, much different energy levels are achieved in CM and SM during the nonlinear stage. Unlike the case LC2 of THM, however, the CM life cycle does decay eventually. While LC2 is associated with a nearly axisymmetric distribution of potential temperature on PV surfaces (Fig. 10 of THM), the PV contours in CM (Fig. 8d) continue to elongate zonally as the eddy slowly loses energy to the zonal mean.

The EKE can change through baroclinic conversion and barotropic decay (Lorenz 1955). The domain-averaged EKE is governed by

$$\frac{\partial \langle K_E \rangle}{\partial t} = C_E - C_Z + D_E, \tag{6}$$

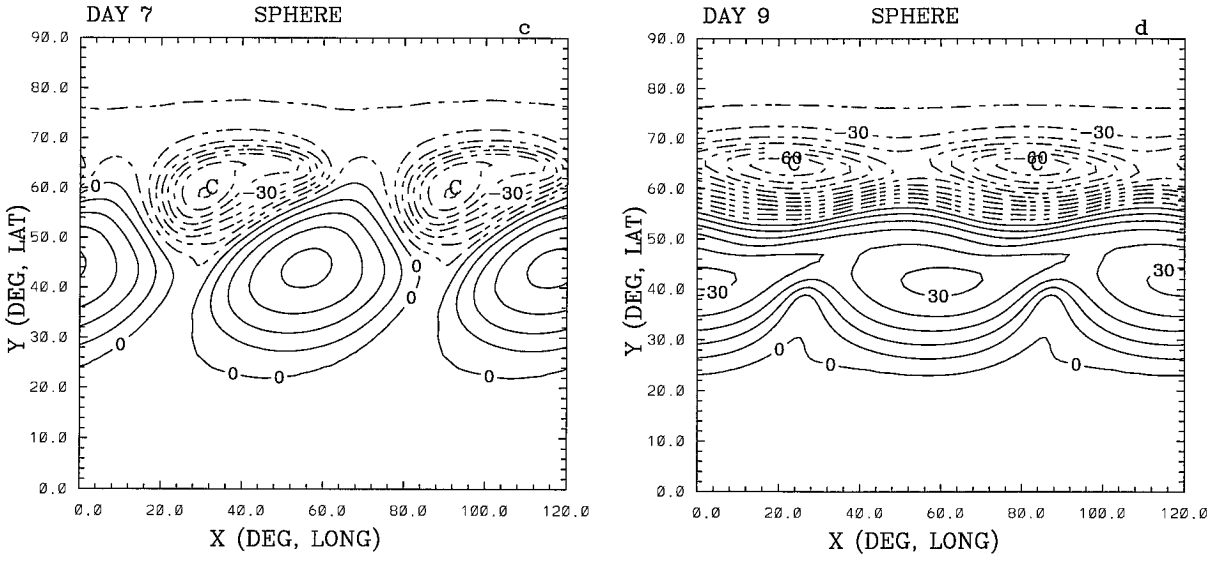

FIG. 6. (*Continued*)

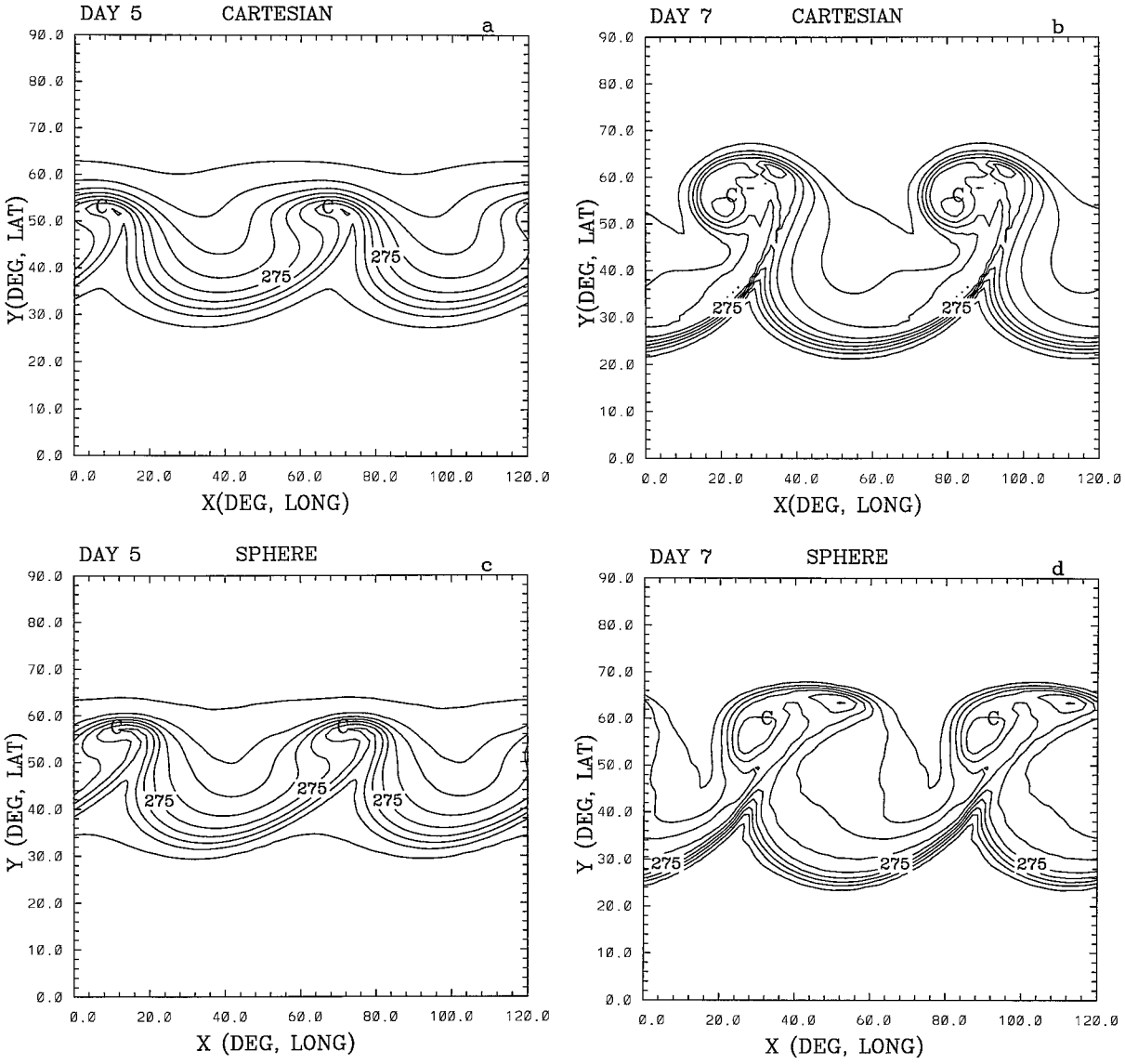

FIG. 7. Temperature field (every 5 K) at 975 mb on days (a) 5 and (b) 7 in the Cartesian geometry. The corresponding fields for spherical geometry on days 5 and 7 are shown in (c) and (d), respectively.

where D_E is dissipation and the two energy conversion terms are

$$C_E = -R \int_0^{p_0} \frac{\{\omega' T'\}}{p}\, dp \tag{7}$$

and

$$C_Z = -\int_0^{p_0} \left\{ \cos\phi\, [u'v'] \frac{\partial([u]/\cos\phi)}{\partial y} \right\} dp$$

$$-\int_0^{p_0} \left\{ [u'\omega'] \frac{\partial [u]}{\partial p} \right\} dp. \tag{8}$$

The square brackets indicate a zonal mean (terms involving gradients of $[v]$ have been omitted). The conversion C_E is from eddy available potential energy (APE) to EKE. The conversion C_Z is from zonal kinetic energy (ZKE) to EKE. In the experiments, D_E was negligible. We will refer to C_Z as the barotropic decay, since it is strongly dominated by the first integral in (8).

In Fig. 12 we have plotted C_E and C_Z as a function of time. The curves for baroclinic conversion (Fig. 12a) are similar in the two simulations, with the peak reached in the spherical simulation being slightly higher than in CM. What mainly distinguishes SM from CM is the onset and the intensity of the barotropic decay. In SM (Fig. 12b), this decay lasts for only 3 days but begins earlier and becomes much more intense than in CM. Note that the early onset nearly coincides with the maximum in baroclinic conversion. This means that the dis-

integration of the SM eddy after day 7 is probably not due to the absence of baroclinic conversion.

According to (8), in the presence of eddy momentum fluxes, energy is exchanged between ZKE and EKE whenever there is mean angular velocity ''shear,'' $([u]/\cos\phi)_y \neq 0$, that is, when the flow departs from solid-body rotation. The barotropic decay term can be expanded as

$$B = -\int_0^{p_0} \left\{ [u'v'] \left([u]_y + [u]\frac{\tan\phi}{a} \right) \right\} dp. \qquad (9)$$

We will refer to the first part of (9) as the ordinary shear effect and the second as the spherical effect. The second term arises because of the convergence of the meridians toward the poles. The magnitude of the spherical effect is usually about 50% of the shear effect overall but can be much larger at some latitudes and times. The spherical effect is plotted separately in Fig. 13. Between days 5.5 and 6.5, the decay in SM is almost entirely due to the spherical effect. On day 8, when the decay is most intense, the spherical effect contributes 1/4 to the total barotropic decay.

Although the length a is considerably larger than the meridional scale of the mean flow, sphericity is important in barotropic decay when the correlation $[u'v']$ is mainly of one sign (like $[u]$), as it is in the SM life cycle. In westerly flow, the spherical effect represents a *loss* of energy when the momentum flux is poleward but allows eddies to *gain* energy from the mean flow if the flux is equatorward.

d. Eddy momentum fluxes and jet migration

As emphasized in the introduction, model differences are also readily apparent in the momentum fluxes. These can be upgradient as long as the waves are growing baroclinically. Although momentum fluxes figure in the barotropic energetics, their main dynamical significance is in the movement of the low-level jet (LLJ). This movement is already underway during the linear period. In Figs. 14 and 15, we have plotted the meridional cross section of the zonally averaged eddy momentum fluxes for CM and SM. We discuss CM first and then SM.

The dominance of equatorward momentum fluxes in CM is established by day 3 (Fig. 14a). The fluxes are concentrated on the cyclonic side of the jet, in agreement with other studies (Snyder et al. 1991; THM; Rotunno et al. 1994), which have shown that the eddies themselves are located on the cyclonic side of the jet. There are two centers, one near the surface and the other near 450 mb. Initially, there is no horizontal shear at the ground, but by day 3 the rectified temperature and PV fluxes have forced a significant surface jet with a small band of poleward momentum flux on its anticyclonic side.

The magnitude of the momentum fluxes increases with time (Fig. 14b). The pattern also changes somewhat, mainly at low levels, where we notice an extension of the equatorward values and a weakening of the poleward values on the anticyclonic side of the jet. By day 7, the surface wave has broken cyclonically, as previously seen in Figs. 5c and 7b, and the low-level fluxes have become erratic (Fig. 14c). The upper-level fluxes, still predominantly equatorward, have amplified considerably. By day 9 (Fig. 14d), the upper-level wave has also saturated (cf. Fig. 8d) and a barotropic pattern of predominantly equatorward flux is established.

In SM (Fig. 15), we at first see upper and lower flux extrema, as in CM. Comparable northward and southward momentum fluxes are converging just poleward of the center of the domain on day 3 (Fig. 15a). This asymmetry is clearer on day 5 (Fig. 15b), when the band of poleward momentum flux is encroaching strongly on the cyclonic side of the jet. On day 7, the barotropic momentum fluxes are more intense than at any time in the CM solution and are everywhere poleward (Fig. 15c). The strong fluxes imply intense barotropic energy transfer. The surface wave breaks soon after this time, as previously seen in Figs. 6c and 7d. The upper-level fluxes are stronger at the time of low-level wave breaking than at the corresponding moment in CM and, accordingly, upper-level wave breaking in SM follows more quickly. By day 9 (Fig. 15d), the upper wave has broken and the fluxes are erratic.

As explained in THM, baroclinic waves saturate first at the low levels. Most of the low-level EKE transfer to the mean flow occurs during a short time at the end of the life cycle. However, interaction between the mean flow and eddies is also taking place earlier (Nakamura 1993). In order to understand the feedback between the mean flow and EKE decay, we consider the time-dependent strength and position of the LLJ. The zonal-mean wind tendency on the sphere is given by

$$\frac{\partial[u]}{\partial t} = -\frac{\partial([u'v']\cos^2\phi)}{a\cos^2\phi\partial\phi} - \left(\frac{\partial([u]\cos\phi)}{a\cos\phi\partial\phi} - f \right)[v] - [\omega][u]_p - [\omega'u']_p + [F_x] \qquad (10)$$

(Andrews et al. 1987). The first two terms on the right normally dominate. The first term is the convergence of angular momentum flux. It can be rewritten as

$$C = -\frac{\partial[u'v']}{a\partial\phi} + \frac{2[u'v']\tan\phi}{a}. \qquad (11)$$

The second part of C, combining a horizontal convergence effect due to sphericity and a ''centrifugal'' effect of exactly the same magnitude, represents the additional mechanism for accelerating the mean jet owing to sphericity. On the sphere, poleward momentum fluxes produce mean zonal acceleration even without meridional mean wind gradients.

During linear development, the mean meridional flow $[v]$ at low levels is approximately proportional to the surface eddy heat flux, which is enhanced by the large

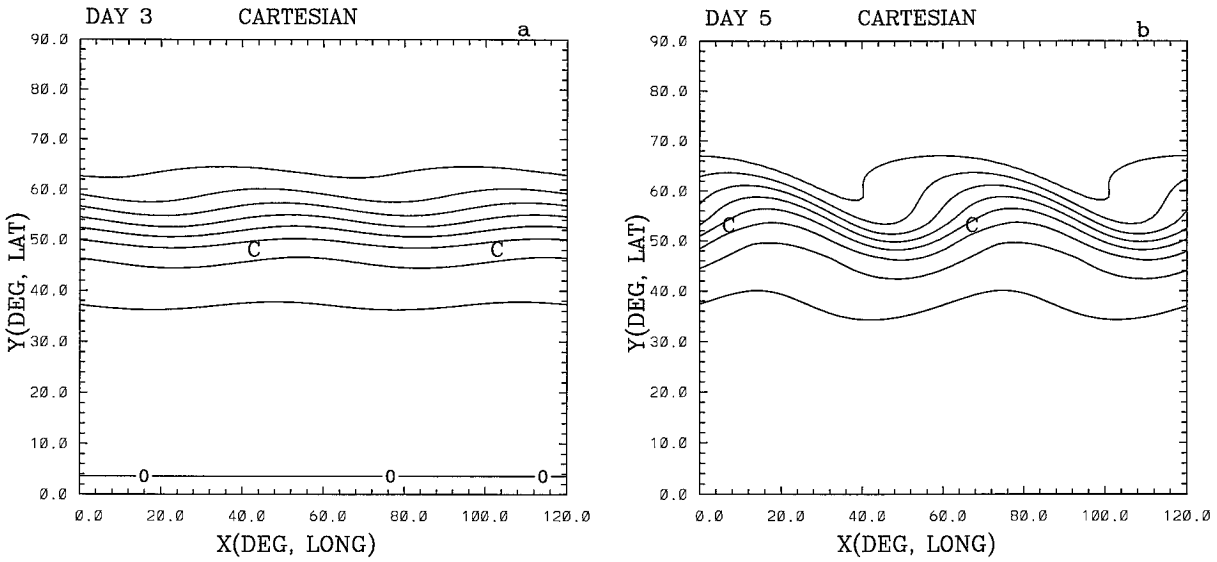

FIG. 8. Potential vorticity evolution on the $\theta = 320$ K surface in Cartesian geometry. The PV fields (every 0.5 PVU) are shown on days (a) 3, (b) 5, (c) 7, and (d) 9.

f on the poleward side. As a result, the mean Coriolis acceleration $f[v]$ tends to establish low-level westerlies somewhat poleward of the baroclinic jet axis (45°) in both CM and SM. The flux convergence implied by Figs. 14 and 15 reinforces this poleward tendency of the LLJ in SM but opposes it in CM, where the maximum convergence is on the opposite side of the jet axis from the mean Coriolis acceleration. This contrast is illustrated schematically in Fig. 16.

We have plotted in Fig. 17 the positions of the maximum westerly wind and the two sources of westerly momentum for CM and SM, along with positions of the low centers at 975 mb. From early on, the LLJ in SM shows a tendency to migrate toward the pole (Fig. 17b), led by the two cooperating momentum sources. By contrast, the jet in CM (Fig. 17a) shows very little movement until the roll-up starts. Although the LLJ does not perfectly track the surface pressure centers, there is also a greater poleward movement of the low-level cyclones in SM in comparison to CM (cf. Fig. 17b). The implied misalignment of upper- and lower-level lows in SM was mentioned at the end of section 3b. In CM, the anticyclones become misaligned.

In Fig. 18, we have plotted the actual mean zonal wind on day 8 in both CM and SM. On account of the strong feedback with the eddy, barotropic conversion on

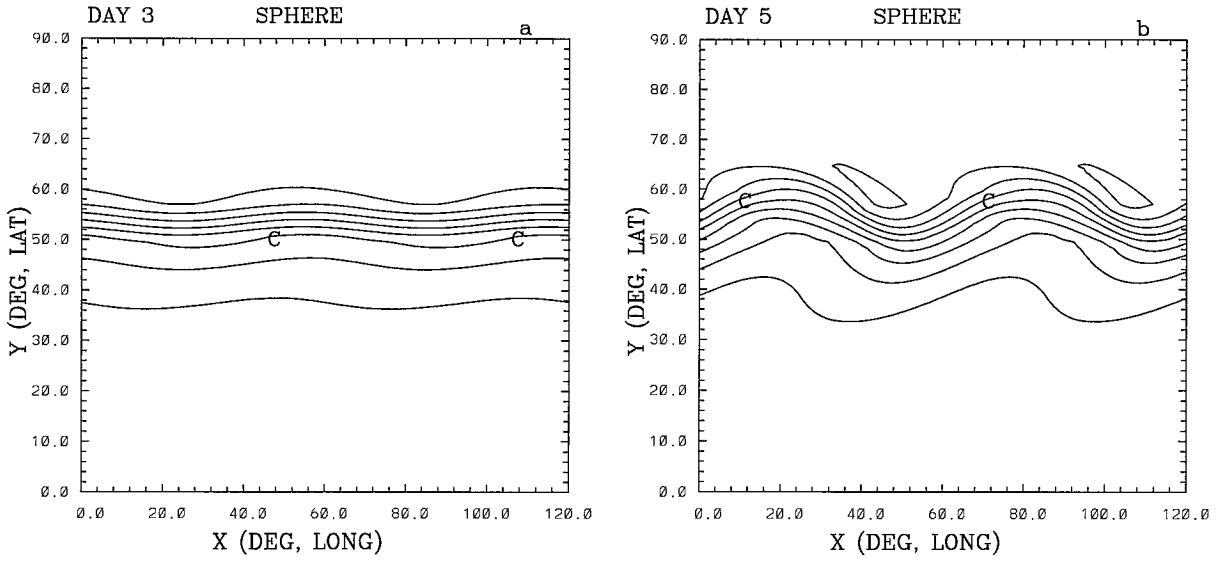

FIG. 9. Same as in Fig. 8 except for the spherical simulation.

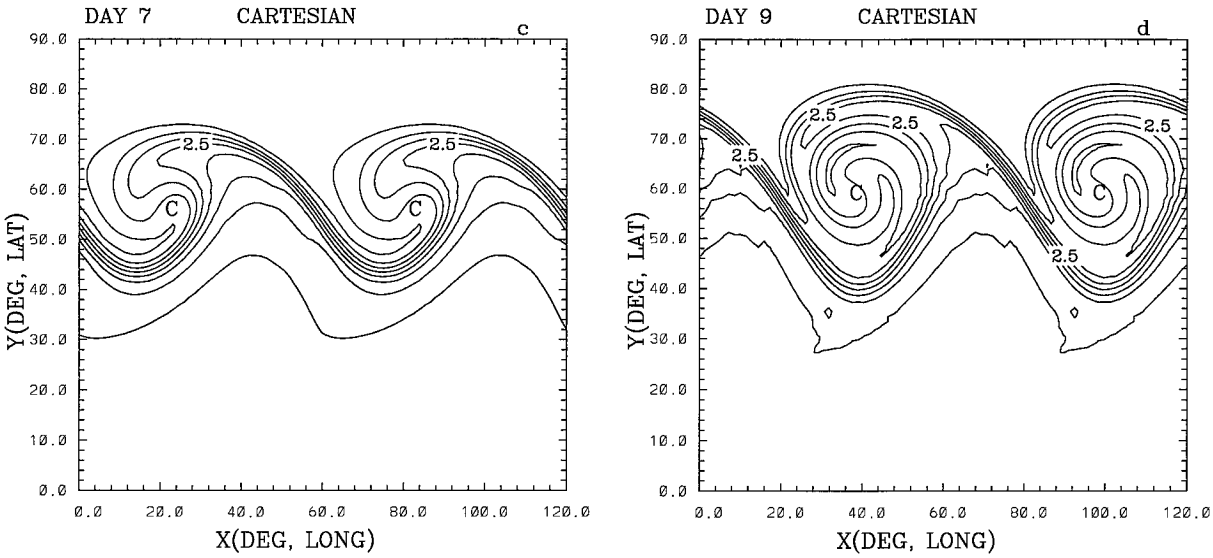

FIG. 8. (*Continued*)

the sphere has established an LLJ of 40 m s^{-1} on day 8 when the corresponding amplitude in CM was only 22 m s^{-1}. Earlier, on day 7.5, the difference was 7.5 m s^{-1} (not shown). We presume that the amplitude of these winds would be significantly reduced in a model with realistic surface friction. The aforementioned massive shift of the jet maximum toward the pole at low levels in SM is also apparent in Fig. 18. The momentum flux convergence eventually dominates the Coriolis acceleration of the zonal flow in SM but never in CM. Whereas substantial baroclinicity is still present in CM, the model atmosphere in SM has become almost barotropic.

The expansion of the anticyclonic region in SM allows the domain-averaged momentum flux on the sphere to surpass that in CM by day 5 (Figs. 14b and 15b). Not only is there more room for poleward flux in the expanded anticyclonic region, but the confinement of the cyclonic shear ultimately leads to poleward (*downgradient*) flux on this side of the jet as well. The downgradient tilt on the cyclonic side is consistent with local barotropic instability. The horizontal length scale, L, of the cyclonic shear is less than 1000 km (60°–70° in Fig. 17b). According to Gill [1982, Eq. (13.6.13)], the flow can become barotropically unstable if $L < \sqrt{\Delta U/\beta}$. This condition is satisfied for $\beta = 10^{-11}$ m^{-1} s^{-1} and $\Delta U =$ 30 m s^{-1}, which are appropriate values for day 7. The

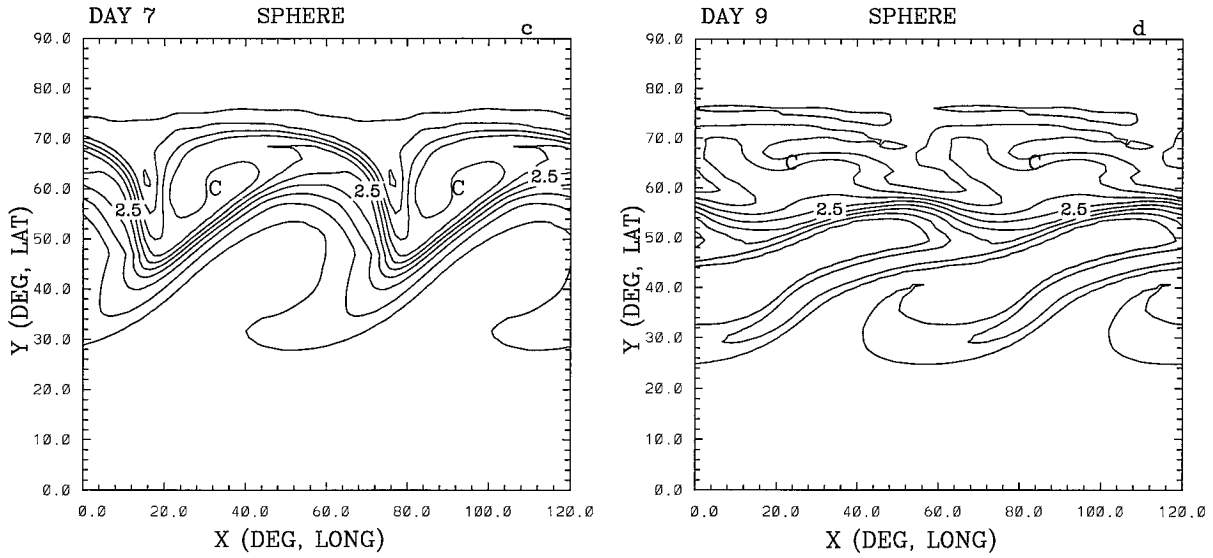

FIG. 9. (*Continued*)

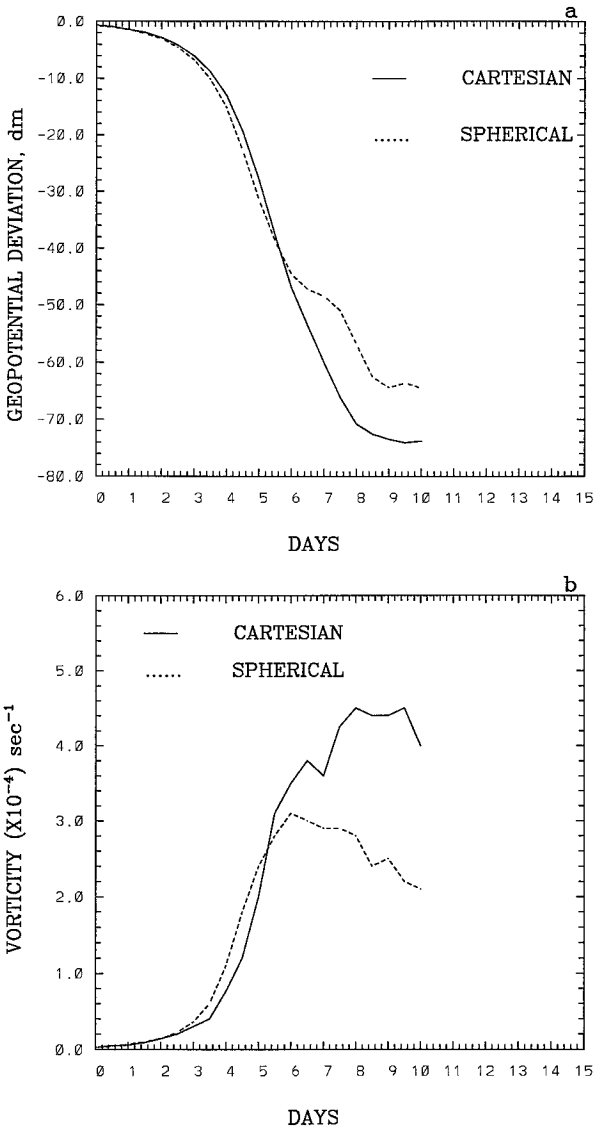

FIG. 10. Evolution of (a) the minimum value of the geopotential departure at 975 mb and (b) the maximum value of vertical component of the relative vorticity at 975 mb for the spherical and Cartesian simulations.

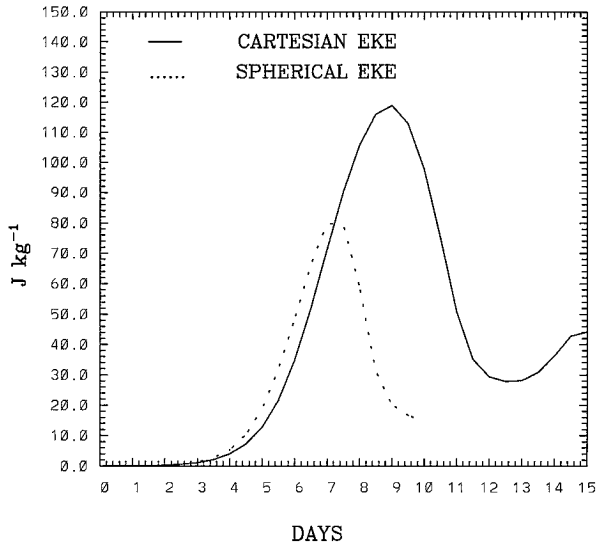

FIG. 11. Evolution of the domain-averaged EKE in the spherical and Cartesian simulations.

zonal scale of wavenumber 6 at this latitude is comparable to the meridional scale of the cyclonic shear, also consistent with barotropic instability. The generation of narrow, barotropically unstable jets on the sphere was also noticed in experiments by Simmons and Hoskins (1978). Held and Andrews (1983) found downgradient fluxes in the case of jet widths smaller than the deformation radius.

Seeking direct confirmation of the barotropic governor (the feedback between the eddy decay and barotropic wind), we conducted an experiment on the sphere in which we turned off the zonal-mean forcing due to eddy momentum flux in the mean zonal momentum equation. Only the acceleration by the meridional circulation and vertical advection were retained. The LLJ migrated to only 50° by day 9 and the zonal flow remained barotropically stable (no downgradient flux). The EKE peaked on day 9 instead of day 7. Most of the difference in the eddy decay term (9) was due to the decrease in $[u_y]$ rather than the decrease in momentum flux. The decay due to the spherical effect was not as strongly affected as the ordinary shear effect. This probably explains why the eddy in this artificial experiment retained its anticylonic tilt and eventually zonalized. This experiment quantifies the importance of feedback in the LC1 equilibration.

To see just how simply the wave equilibration could be represented, we also ran the spherical experiments with only zonal wavenumbers 0 and 6 retained. Even though north–south-oriented frontal structures were thus eliminated, the simple wave–mean flow experiment yielded essentially the same wave breaking and roll-up processes as in the full model. The principal difference was seen in LC2 after the peak in EKE: in the severely truncated LC2 solution, the vortices never became fully symmetric and eventually zonalized, rather as in CM.

e. Barotropic decay

Now we return to the barotropic decay process and consider the spatial distribution of the barotropic decay terms in the EKE tendency equation. With the purpose of relating domain-averaged EKE changes to local changes in mean flow, we use the form given by Andrews et al. (1987); namely,

$$\frac{d[K_E]}{dt} = -[u'v']\left(\frac{\partial[u]}{a\partial\phi} + \frac{[u]\tan\phi}{a}\right) - \frac{R[\omega'T']}{p} - \frac{\partial\cos\phi[\phi'v']}{a\cos\phi\partial\phi} - \frac{\partial\omega'\phi'}{\partial p}, \quad (12)$$

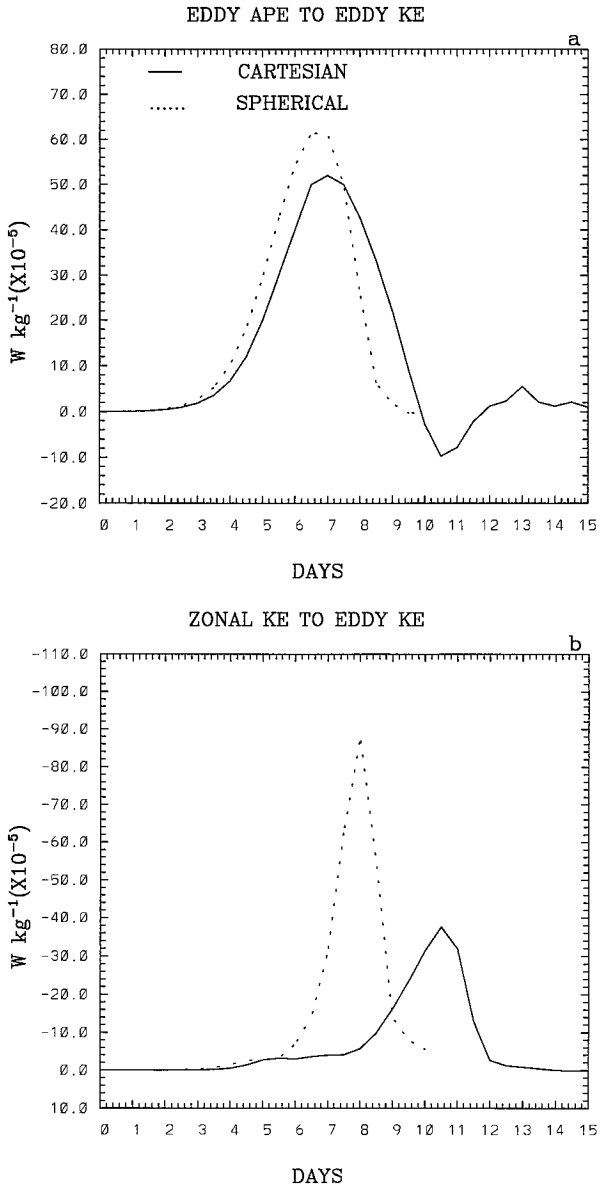

FIG. 12. Evolution of the domain-averaged (a) baroclinic conversion and (b) barotropic decay for the spherical and Cartesian simulations.

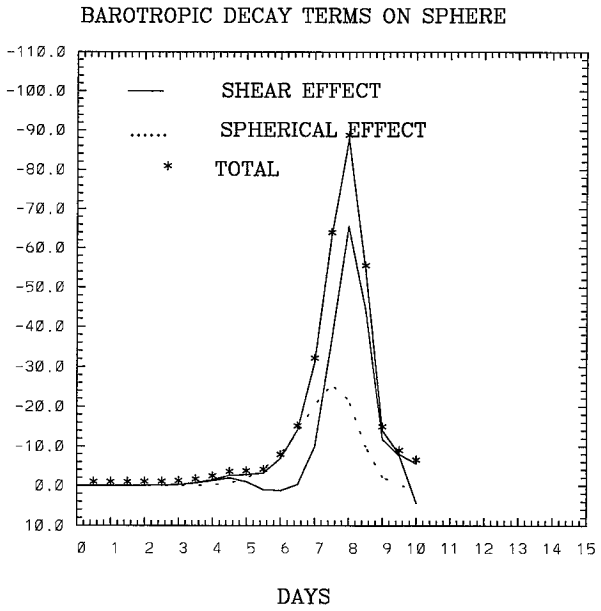

FIG. 13. Evolution of the domain averaged total barotropic decay and the contribution from shear and spherical metric terms.

where $(d/dt) = (\partial/\partial t) + [u](\partial(a\cos\phi)/\partial\lambda)$. The first term on the right of (12) is the barotropic decay term and the second is the baroclinic conversion term. The last two terms are the geopotential flux convergence, which averages to zero over the domain. If the horizontal flux is rewritten to include the meridional kinetic energy flux, the barotropic decay becomes

$$\frac{d[K_E]}{dt} = [u]\left(\frac{\partial[u'v']}{a\partial\phi} - 2\frac{[u'v']\tan\phi}{a}\right) + \cdots. \quad (13)$$

The quantity in parenthesis occurs with opposite sign in the zonal momentum tendency equation (10). However, since the horizontal flux convergence in (13) involves the mean flow and largely offsets the conversion terms, we prefer (12).

Since the barotropic decay depends on both the momentum flux and angular velocity shear, the feedback in the barotropic governor can operate through the time dependence of either the mean wind or the tilt of the eddy. Given the relationship between horizontal shear and meridional tilt of baroclinic waves, both feedbacks tend to be positive.

In Fig. 19, we have plotted the shear term of the barotropic decay for CM and SM on days 5 and 7. In the CM solution (Figs. 19a,b), we at first see eddy decay due to the upgradient fluxes on the cyclonic side of the jet. Then by day 7, the maximum decay has shifted to the upper troposphere, and weak positive values appear at low levels. The positive values are associated with a wobble in the surface cyclones, seen in Fig. 5c. This interesting feature lasts only a day or so and may be part of a filament-shedding process that symmetrizes the eddies following the wave equilibration.

For SM, day 5 follows by about a half day the downturn in domain-averaged barotropic decay due to shear (cf. Fig. 13). We can now confirm that the downturn is associated with strong downgradient momentum flux on the cyclonic side of the jet, mainly at low levels (Fig. 19c). The jet maximum is still equatorward of 50°, but the poleward momentum flux extends to 58° (cf. Fig. 15b). As suggested in section 3d, the pattern of downgradient fluxes is sufficiently strong and persistent to be considered a barotropic instability, made possible by the sharpening of the cyclonic shear during the poleward jet migration. By day 7, the positive contribution to eddy energy by the shear no longer exceeds the negative con-

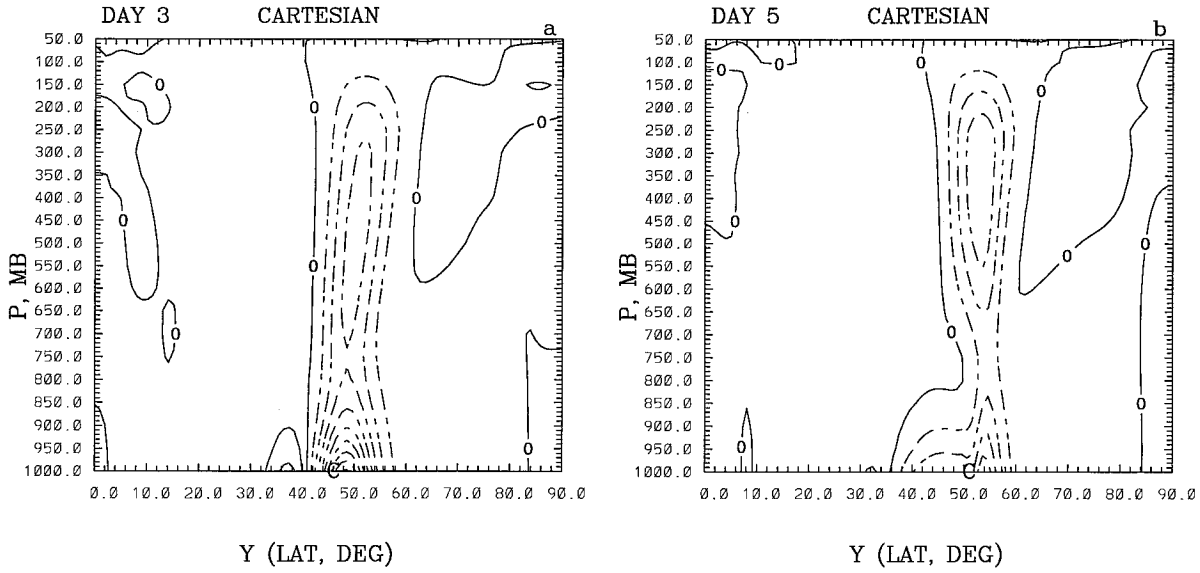

FIG. 14. Meridional cross section of horizontal eddy momentum fluxes in the Cartesian simulation on days (a) 3, (b) 5, (c) 7, and (d) 9. The contour interval is 1 $m^2 s^{-2}$ for (a) and 10 $m^2 s^{-2}$ for (b), (c), and (d).

tribution. By day 8 (not shown), the band of downgradient flux is squeezed out completely and decay due to zonal-mean shear fills the whole cross section.

In contrast to the shear term, the spherical term always leads to decay of the eddy. As shown in Fig. 20, the spherical term is largest where the winds are strongest. Since the zonal winds are in general westerly, the sign of the term is decided by the direction of the momentum fluxes. As previously seen in Fig. 13, barotropic decay due to the spherical effect becomes most important during days 5–7, the period of low-level wave breaking. During this period, the net shear term contribution is small, but the surface westerlies and meridional eddy tilt continue to increase. This augments the importance of the spherical effect in the feedback between the momentum flux and mean wind. The flux divergence (not shown) is of the same order of magnitude as the other terms in (12) but is rarely large enough to change the sign of the EKE tendency. This is part of the reason for preferring (12) over (13). In the latter equation, the flux terms change the sign of the tendency at the latitudes of negative ZKE tendency in SM.

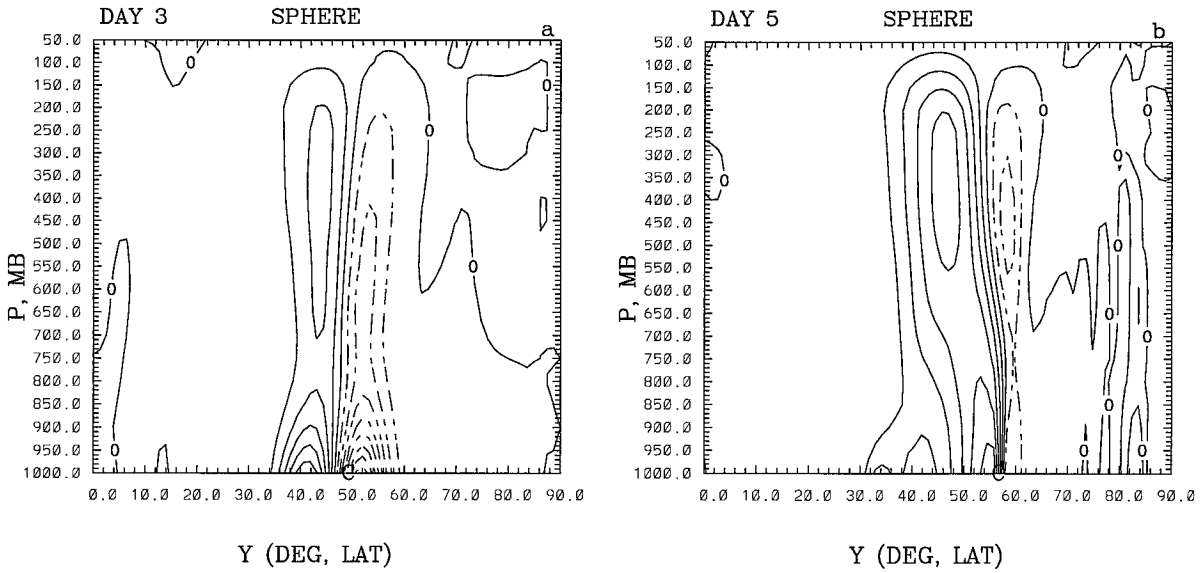

FIG. 15. Same as in Fig. 14 but for the spherical simulation.

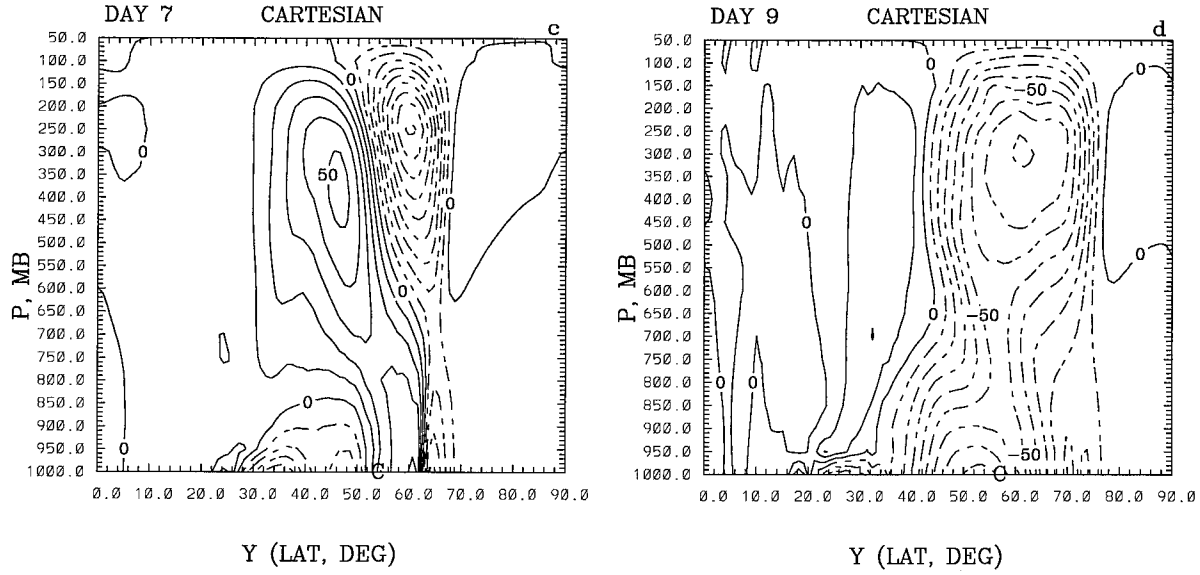

FIG. 14. (*Continued*)

4. Special experiments

a. Cyclonic roll-up in spherical geometry

As mentioned in section 3, the CM life cycle resembles in almost all respects THM's cyclonic life cycle, LC2. The latter is obtained by adding cyclonic barotropic shear to the basic flow in an otherwise standard SM life cycle simulation. Although THM deemphasized the differences during linear development between LC2 and the control LC1, we will see that the structure of the momentum fluxes is quite different in the early stages. As in the contrast between SM and CM, we believe it is the weaker feedback between the eddy momentum fluxes and the mean zonal wind *during the linear stage* that makes the nonzonalizing life cycle possible on the sphere. THM used EP flux diagnostics to contrast LC1 and LC2. Since EP flux diagrams are dominated by heat fluxes at early times, this approach automatically conceals important differences during the linear growth period.

To reproduce LC2, we added a cyclonic barotropic shear similar to THM: a sinusoidal profile with maximum westerlies of 10 m s^{-1} at 20° and maximum easterlies of 10 m s^{-1} at 50°. The normal mode for this basic

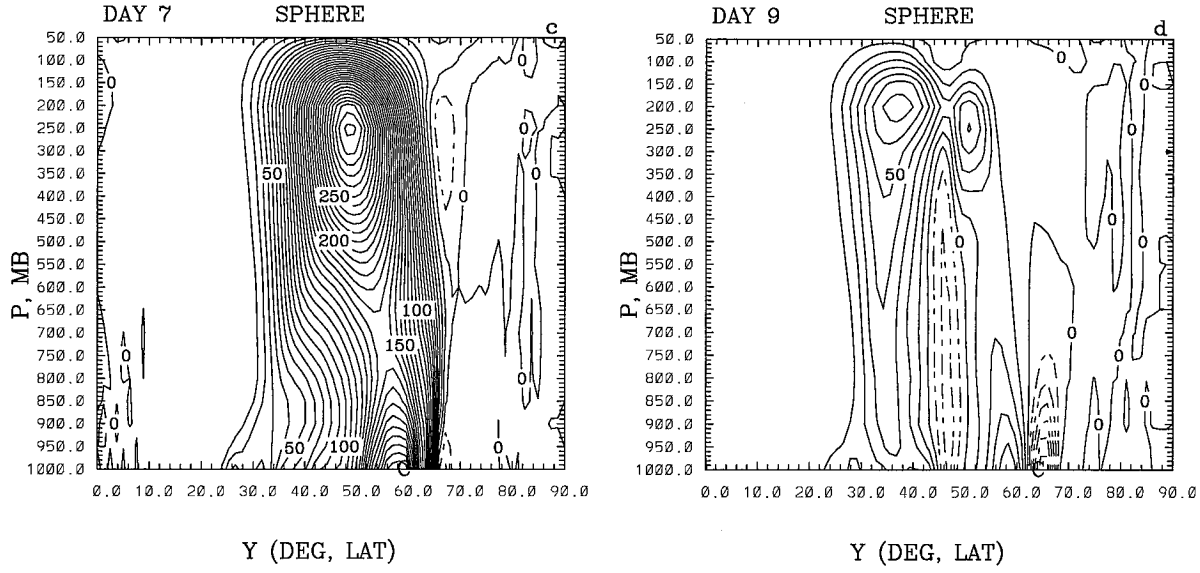

FIG. 15. (*Continued*)

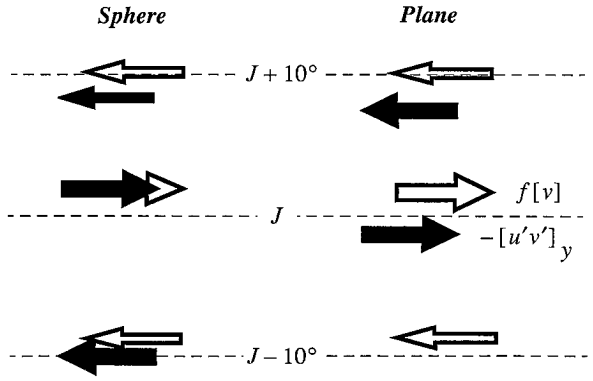

FIG. 16. Schematic illustration of the two momentum forcings at low levels during the linear development in SM (left) and CM (right). The dark arrows refer to the eddy momentum flux convergence, and the open arrows refer to the Coriolis acceleration. The label "*J*" indicates the position of the jet axis, which is at 45° in the present experiments.

state is shown in Fig. 21 and can be compared with that of the control run (LC1) in Fig. 3b. The NW–SE bias in the horizontal tilt of the LC2 solution is even more striking than that of the CM solution (Fig. 3a). Only the upper levels show any sensitivity to the anticyclonic shear on the equatorward side of the jet. The meridional cross section of the normal-mode horizontal eddy momentum fluxes (Fig. 21b) is qualitatively similar to that of the CM solution (Fig. 4a). The growth rate of the LC2 normal mode is reduced to 0.60 day^{-1} (0.71 day^{-1} without the cyclonic shear), in agreement with THM. The phase speed is 5.7° day^{-1}. The synoptic evolution and upper-level equilibration of this cyclonic life cycle are described in detail in THM. Here we focus on eddy momentum fluxes and the consequent barotropic decay.

The main observation is that the eddy momentum fluxes remain predominantly equatorward throughout the simulation (not shown). They have nearly vanished by day 7, at which time the low-level cyclone center has barely reached 49° (cf. the position of the label "C" in Fig. 15c). The full disturbance is sharply confined in the meridional direction. These results are all similar to CM (Figs. 14b and 14c). A further implication of the equatorward momentum flux is that the spherical curvature contribution (whose magnitude is generally 50% of the shear term) in (12) now acts to convert energy from mean flow to eddy. The end product of the development is quasi-steady, equivalent-barotropic vortices with little barotropic decay. As in CM, the lows produced by this occlusion process are more barotropic than the highs, as the cyclones are better aligned in the vertical than the anticyclones. The difference is still not as striking as in LC1, however.

THM used Rossby wave radiation theory to show that a refractive index barrier exists in the upper troposphere to prevent the radiation of wave activity to the subtropics in LC2. Our original basic zonal wind differs at upper levels from that of THM (cf. our Fig. 1a and THM's Fig. 3a). THM specified a more realistic profile in the stratosphere, whereas our atmosphere is barotropic above the tropopause. For the present atmosphere, we computed the Rossby wave refractive index *K* given by THM's Eq. (10). Since the zonal wavenumber is 6, values of *K* less than 6 correspond to imaginary total wavenumber in the meridional plane. We find centers of minimum *K* in the subtropics in the control spherical simulation LC1 (not shown) and also LC2 (Fig. 22) on day 0 as well as day 5. However, unlike THM, we find no values of *K* less than 6 in the subtropics in LC2. We

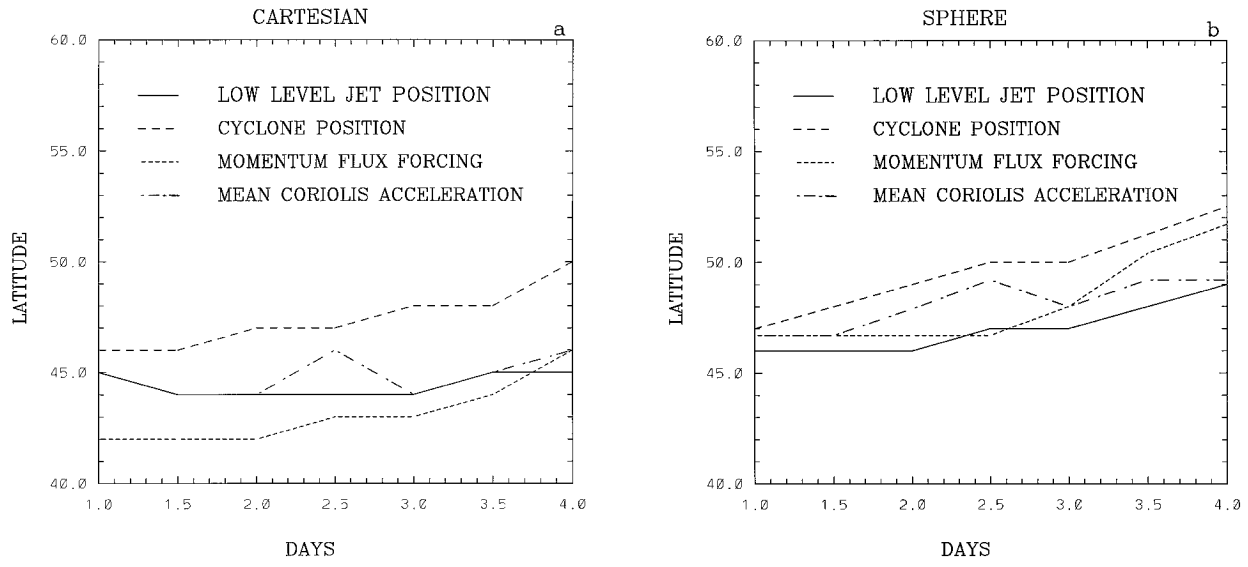

FIG. 17. Meridional positions of the maximum westerly wind at 1000 mb, the maximum momentum forcings (flux convergence and Coriolis), and the surface cyclones in the spherical and Cartesian simulations, plotted as a function of time up to the time of low-level saturation.

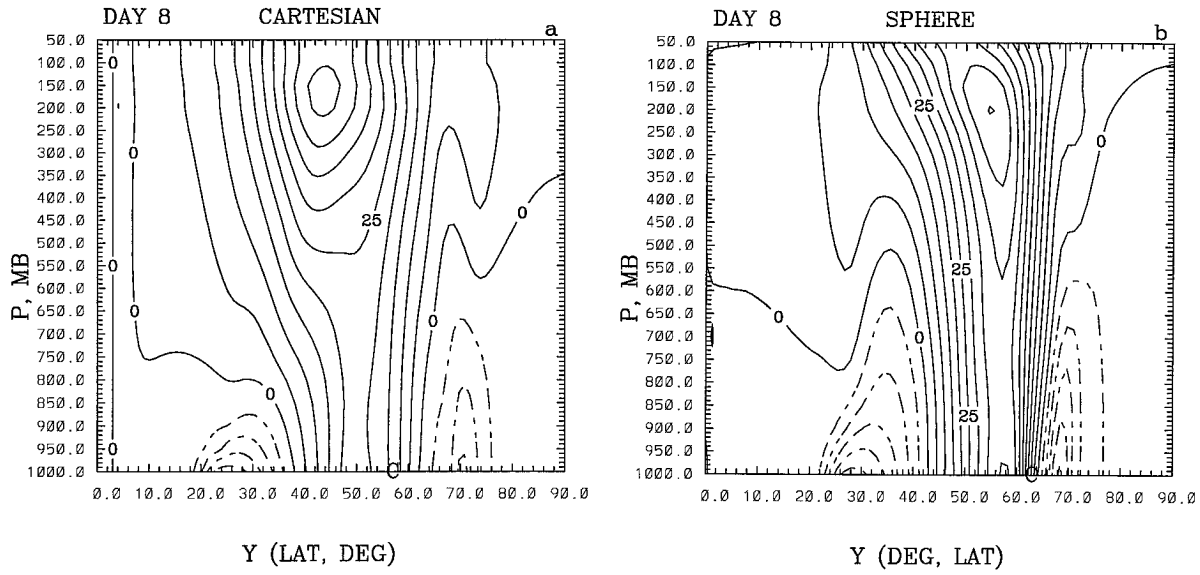

FIG. 18. Meridional cross section of the zonal-mean wind on day 8 in (a) Cartesian and (b) spherical geometry. The contour interval is 5 m s^{-1}.

emphasize that the discrepancy, which is due to the slightly different initial conditions and vertical resolution, does not significantly alter the life cycle. Recently, Lee and Feldstein (1996) analyzed the refractive index in GCM data using a more general definition of *K*. They found significant differences in this measure between cyclonically and anticylonically breaking wave packets, but we do not see a wave activity ''barrier'' in their composite analysis of cyclonic cases.

We experimented with different amplitudes and locations for the cyclonic barotropic shear. In many cases, the normal modes exhibited predominantly equatorward momentum fluxes, and barotropic decay was delayed. However, these cases were not always classifiable as LC2 because sufficient poleward flux developed during the nonlinear stage to prevent the emergence of coherent vortices. In one experiment, we slightly amplified the cyclonic barotropic shear and confined it to latitudes north of the baroclinic jet axis. Even though the Rossby wave refractive index in this initial state was identical to that of LC1 everywhere south of the jet axis, the life cycle was unambiguously of the LC2 type. When we turned off the momentum-flux forcing of the zonal-mean wind, there was no qualitative change in the LC2 development, unlike the drastic effect on LC1 described in section 3.

Between days 9 and 15, the LC2 vortices lose only about one-third of their kinetic energy, whereas the CM vortices lose more than two-thirds of theirs (cf. Fig. 11). We compared upper-level isentropic PV maps like the one in Fig. 8d for the two cases (THM's Fig. 10, showing potential temperature on a PV surface, is a good surrogate for LC2). In addition to the fact the CM eddies span more latitudes, we noticed that the LC2 eddies are more completely pinched off from the high-PV reservoir from which they formed. This seems consistent with the greater steadiness of the SM solution, but it is not clear whether the size of the eddies, the model geometry, or some other effect directly accounts for the slightly different isentropic PV patterns.

b. Anticyclonic roll-up in Cartesian geometry

We next present a Cartesian simulation with poleward momentum fluxes. Davies et al. (1991) demonstrated the profound influence of uniform background shear on the variety of possible fronts and cyclones. They used a semigeostrophic model to illustrate cyclonic wave breaking in cyclonic mean barotropic shear and anticyclonic breaking in anticyclonic mean shear. The present CM possesses none of the symmetries of the quasigeostrophic model (Nakamura 1993) or semigeostrophic model (Davies et al. 1991). However, the arguments given by Davies et al. (1991) suggest that an additional anticyclonic barotropic shear on the cyclonic side of the baroclinic jet in CM will lead to an unusual anticyclonic tilt of the modes and poleward momentum fluxes.

To produce anticyclonic roll-up in CM, we therefore add a barotropic wind profile of the form $u = u_0 \sin \cdot(2\pi\phi'/\phi_0)$ to the basic flow between 45° and 75°. Here $\phi' = \phi - 45°$ and $\phi_0 = 60°$. We choose $u_0 = 10$ m s^{-1}. The modal growth rate is similar to the control run in the Cartesian model (growth rate of 0.66 vs 0.68 day^{-1}). However, the synoptic evolution resembles the control solution in SM and the anticyclonic life cycle discussed in Davies et al. (1991) and THM. In particular, the LLJ moves to the north because of poleward momentum fluxes.

The geopotential deviation at 975 mb on day 7 (not

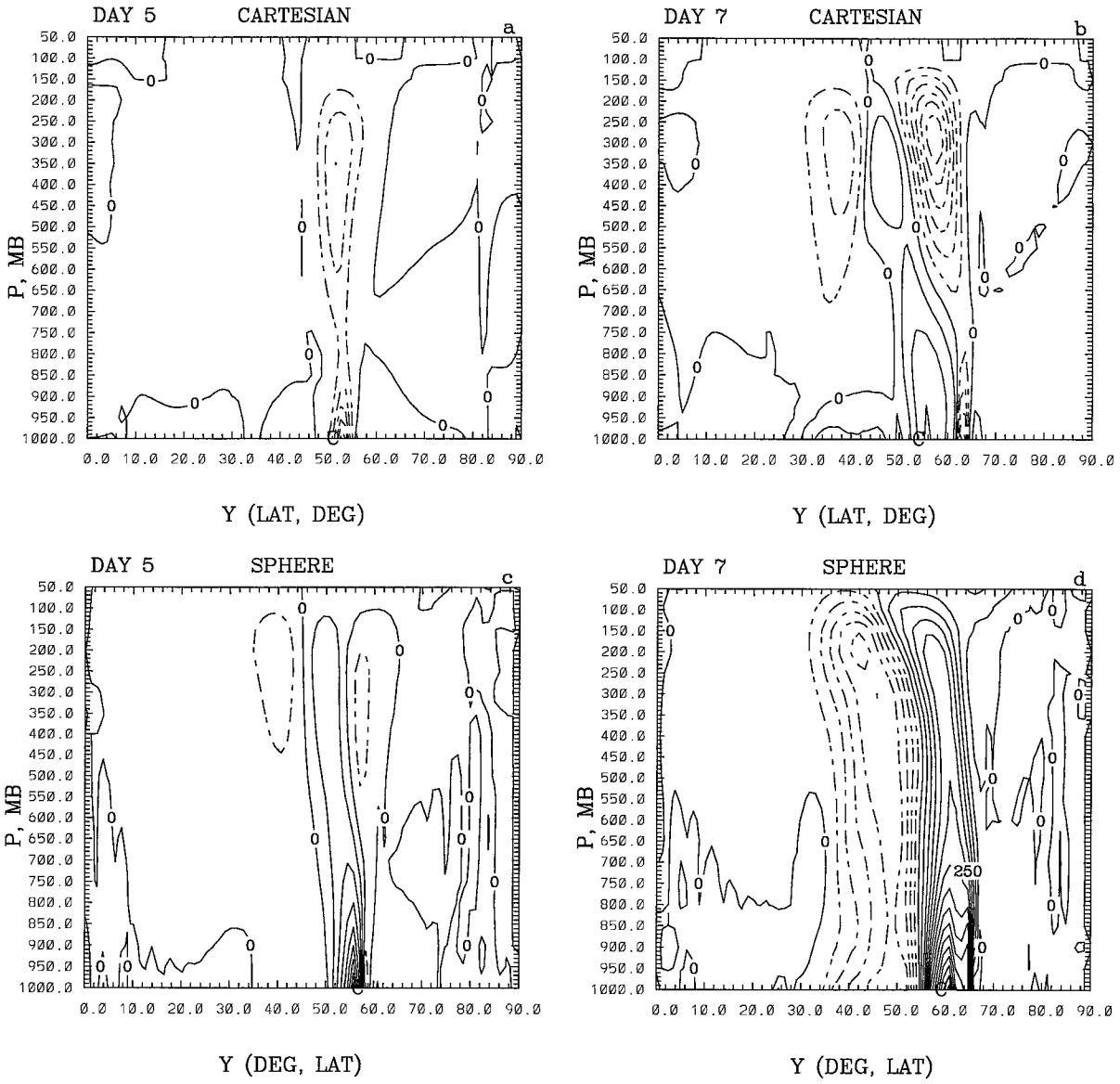

FIG. 19. Meridional cross section of the barotropic decay due to the horizontal shear in the mean zonal wind on days (a) 5 and (b) 7 in the Cartesian simulation. The corresponding fields in the spherical simulation are shown in (c) and (d). The contour interval for (a) and (c) is 2.5×10^{-4} W kg^{-1} and for (b) and (d) is 5.0×10^{-4} W kg^{-1}.

shown) showed that the cyclones were stronger than the anticyclones (in contrast to the semigeostrophic anticyclonic shear case of Davies et al. 1991), and they were smaller than in the control run of CM. There was a general poleward migration of the eddies compared to the CM control (Fig. 17a). The eddies had NE–SW orientation, implying poleward momentum fluxes. The maximum EKE was reached on day 9 (similar to the CM control) and was comparable to that obtained in the CM control (103×10^{-5} vs 112×10^{-5} J kg^{-1}). The decay of the CM anticyclonic eddies was slow compared to LC1, probably because of the missing metric part of the forcing in (9).

c. Easterly jet in spherical and Cartesian geometries

WS found that in westerly basic shear, cyclones are weaker than anticyclones on the sphere and stronger in Cartesian geometry. They showed that with an easterly basic jet, the developing cyclones become stronger than the anticyclones as the former move equatorward. Contrasting this with their westerly jet experiment, they argued that the scale effect (variable length of latitude circles) now operates in favor of the cyclones on the sphere. As noted in section 3c, the difference in the strength of the closed circulations due to geometry is very slight in the multilevel model until the time of low-

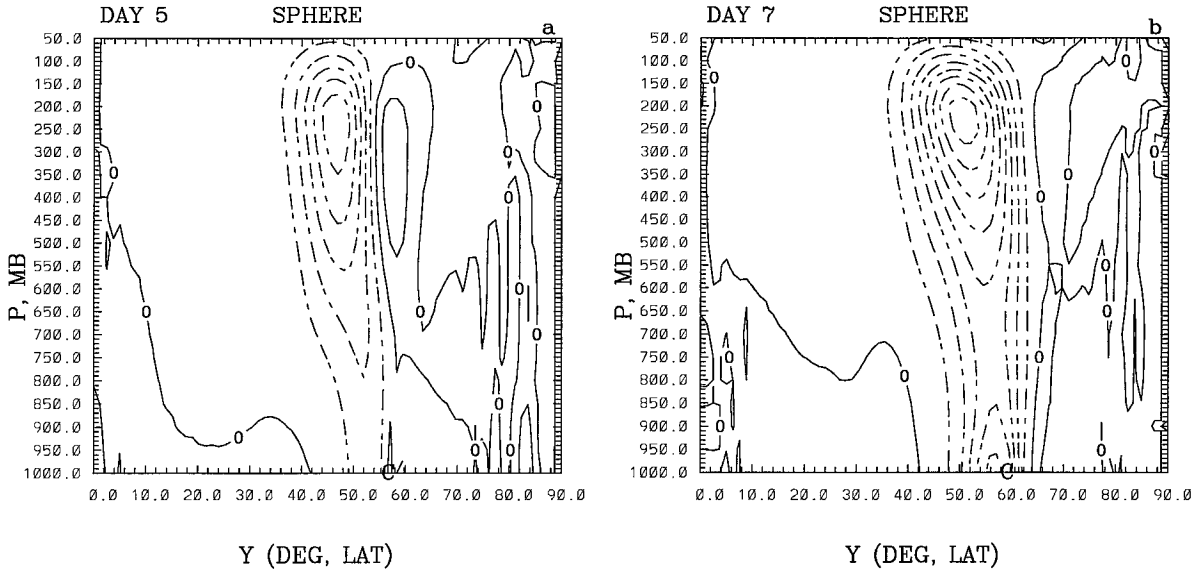

FIG. 20. Meridional cross section of the barotropic decay due to the metric term in the spherical geometry on days (a) 5 and (b) 7. The contour interval is 2.5×10^{-4} W kg^{-1}.

level saturation. The main distinguishing features are the normal-mode momentum fluxes and rate of eddy decay (much faster on the sphere). In this section, we briefly describe the results of experiments conducted with an easterly basic state in Cartesian and spherical geometries.

Changing to an easterly basic state reverses the temperature gradient on the lower surface, while the planetary vorticity gradient does not change sign. Since the upper lid is isentropic, instability then depends on the reversed meridional temperature gradient on the tropopause; accordingly, the linear growth rates decrease considerably. To compensate, we increased the maximum jet speed from 47.5 m s^{-1} to 54.5 m s^{-1} at 175 mb and decreased slightly the static stability in the lower troposphere. Again, we used identical PV distributions in the spherical and Cartesian models.

The easterly jet normal modes have growth rates of 0.79 day^{-1} and 0.85 day^{-1} in SM and CM, respectively. We now get predominantly equatorward momentum fluxes in *both* geometries, not just in the CM experiment. Since the angular momentum surfaces always tilt toward the cyclonic side of the upper-level jet and since the horizontal shear is reversed, the equatorward momen-

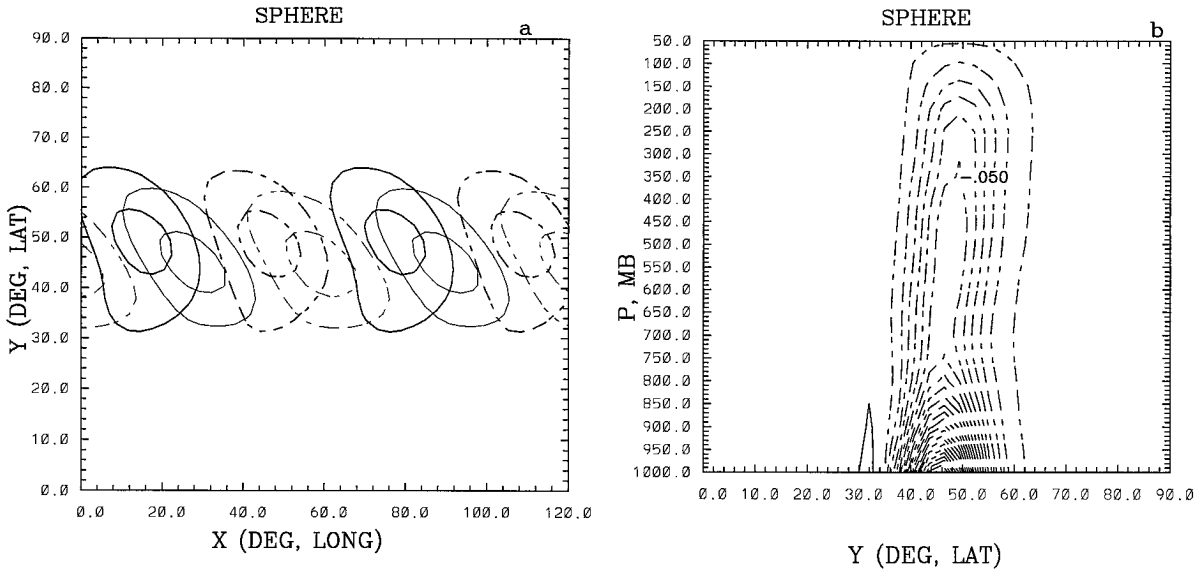

FIG. 21. (a) Meridional velocity (every 0.5 m s^{-1}) of the normal mode at 975 mb (thin lines) and 325 mb (thick lines) for LC2. (b) Meridional cross section of the zonally averaged horizontal eddy momentum flux (every 0.015 m^2 s^{-2}) in the normal mode.

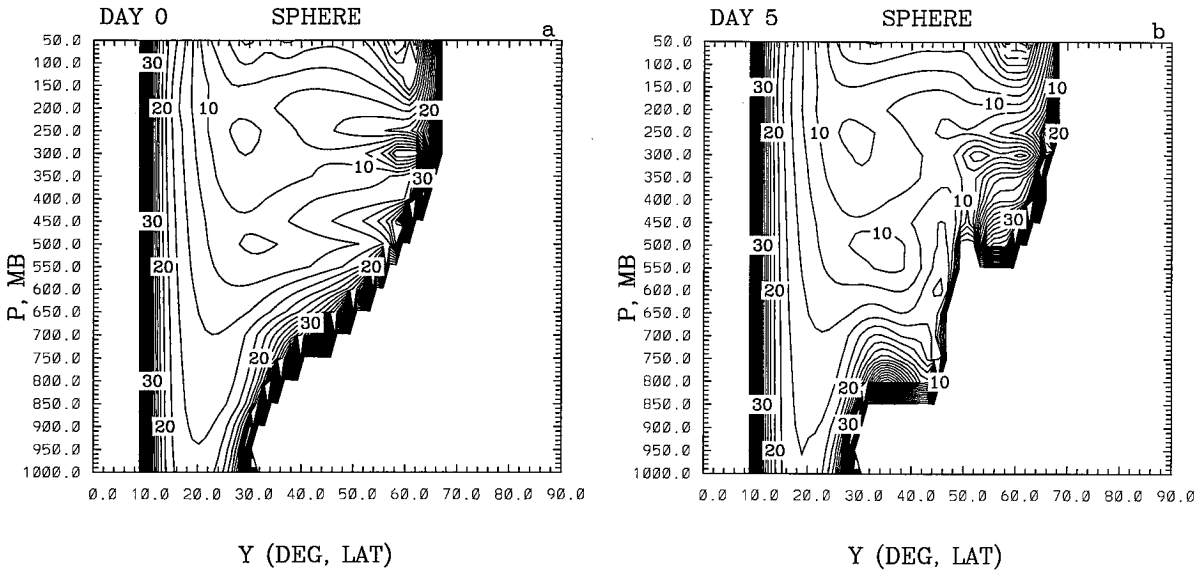

FIG. 22. The Rossby wave refractive index K as given by THM's Eq. (10) on days 0 and 5 for LC2 with the basic state discussed in section 4a.

tum fluxes in CM were expected. The reversal of momentum flux in SM is consistent with the brief heuristic argument offered in section 3a.

Since the temperature gradients are reversed on the lower boundary, the cyclones move equatorward and the anticyclones poleward by about 10° in CM and 5° in SM. In Fig. 23, we have plotted the geopotential deviation at the cyclone center and the domain-averaged EKE as a function of time. Since the growth rates are slightly higher for both SM (0.71 vs 0.78 day^{-1}) and CM (0.68 vs 0.85 day^{-1}), the maximum deepening of the cyclones is greater than in the control experiments (Figs. 10 and 23a). However, the qualitative nature of the curves is the same for easterly and westerly basic shear, if we control for geometry. The EKE evolution is also qualitatively the same (Figs. 11 and 23b) for spherical geometry. The curvature contribution to the decay feedback in SM is still positive for the easterly jet because the zonal-mean flow and momentum fluxes are simultaneously reversed. However, the EKE curve for Cartesian geometry now more closely resembles the case LC2 of THM.

5. Conclusions

Our main objective has been to understand the essential differences in the evolution of baroclinic waves in spherical and Cartesian geometry, starting with normal modes in zonally symmetric basic states. Whitaker and Snyder (1993) had the same purpose in their recent study using a two-layer isentropic model. Relying on vorticity inversion, they showed that the displacement of highs and lows associated with the development of low-level westerlies tended to favor anticyclonic gyres on the sphere. Looking for a more robust mechanism and one that would account for both anticyclonic *and* cyclonic wavebreaking on the sphere, we have focused on the part of the wave–mean flow interaction that involves a positive feedback, namely, the interaction between momentum fluxes and mean meridional shear. Thus, referring to the tendency equations for zonal-mean wind and EKE, we argued that that the momentum fluxes at small amplitude already ensure the dominance of cyclonic or anticyclonic gyres and zonal-mean shear during finite-amplitude development. We believe that, because of the feedback, the meridional tilt of the eddies is more likely to be at the root of the different equilibration outcomes than the relative strengths of the meridionally separated positive and negative streamfunction centers.

The cyclonic life cycle LC2 is obtained on the sphere by adding a cyclonic barotropic shear to the initial flow. This alteration turns the normal-mode momentum fluxes toward the equator, so that the evolution resembles that of the Cartesian control case in many respects. The addition of an *anticyclonic* barotropic shear on the cyclonic side of the baroclinic jet in CM leads to poleward momentum fluxes. The LLJ moves poleward and the barotropic cyclonic shear region is squeezed out. The waves break anticyclonically. The synoptic evolution looks similar to the control case (LC1) on the sphere. However, since the feedback between the barotropic eddy momentum fluxes and the mean flow is generally weaker in Cartesian geomtery, the barotropic decay sets in about as late as in the cyclonic CM roll-up. The principle that eddies decay faster on the sphere also applies to the easterly jet experiments in SM and CM.

We suggest that the low-level barotropic feedback is

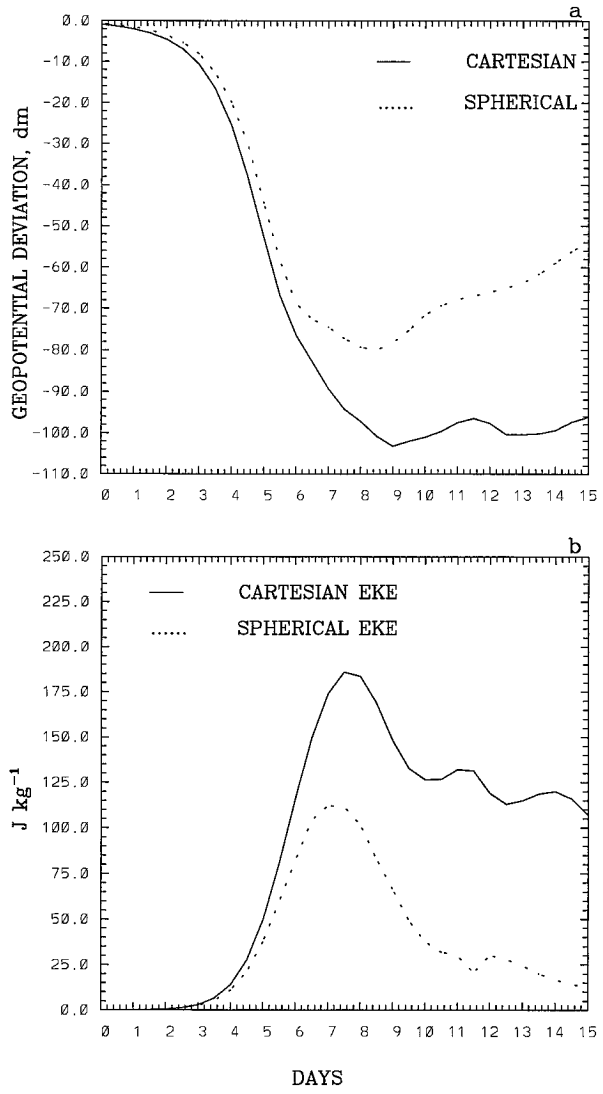

FIG. 23. Evolution of (a) the minimum value of the geopotential departure at 975 mb and (b) the domain-averaged EKE in spherical and Cartesian geometries with an easterly shear basic state.

also part of the explanation for the longevity of the nonlinear eddies. The barotropic governor is stronger on the sphere largely because of cooperation with the meridional circulation. This not only hastens the jet creation but also allows the LLJ to move steadily poleward, squeezing out the cyclones and expanding the zone of anticyclonic barotropic decay. Any tendency for equatorward migration of the LLJ in CM is opposed by the mean meridional circulation. In what may be only a second-order effect, sphericity allows an EKE sink and ZKE source in the presence of poleward momentum fluxes regardless of the sign of the zonal-mean shear. In SM, the eddy eventually tilts against the shear on the cyclonic side of the LLJ to produce poleward fluxes everywhere. This allows the spherical metric term to accelerate the mean wind where it is already a maximum, adding a significant (though perhaps not critical) contribution to the eddy collapse after day 6. By contrast, domain-averaged barotropic momentum fluxes in CM are still negligible on day 7. The weaker barotropic decay in that model allows the cyclonic eddies to ''symmetrize'' into coherent vortices at a crucial time when baroclinic conversion is on the decline.

We have tried to relate our view of normal-mode equilibration to that of THM, since their study of the sensitivity to initial barotropic shear in the spherical model seems to parallel our investigation of differences due to geometry. The EP flux divergence in our LC1 and LC2 is essentially the same as theirs, but we find no refractive index barrier in the various LC2 or Cartesian experiments to account for the emergence of long-lived vortices in terms of neutral Rossby wave radiation. Nor could we find a barrier in the refractive index plots by Lee and Feldstein (1996) based on recent GCM data. Feldstein and Held (1989) concluded that Rossby wave radiation had a negligible to small effect on ''moderately supercritical'' life cycles, depending on the proximity of the linear critical latitudes to the jet axis. Our experiments appear to fall into this category.

As stipulated by THM, the transfer of wave activity implied by EP flux is not automatically attributable to neutral wave radiation, especially across the narrow zone spanned by the present sort of eddies. Wave activity, A, is related to the zonal-mean wind by

$$\frac{\partial A}{\partial t} = -[v'q'] = -\frac{\partial [u]}{\partial t} + fv^*, \tag{14}$$

where v^* is the ''residual'' mean meridional circulation. In our interpretation, the important differences in EP flux divergence, that is, $[v'q']$, between LC1 and LC2 are due to momentum fluxes in either weak or strong self-interaction of the original wave. The overriding importance of the momentum fluxes was verified by removing eddy momentum forcing of the mean zonal wind and finding a major impact on the barotropic decay of LC1. The importance of self-interaction of the fundamental wave was verified by running wave–mean flow versions of the SM experiments and finding only minor changes in the character and timing of the equilibration. Also, we believe it is impossible to understand the different equilibration scenarios without considering the details of the meridional circulation, v^*. This circulation controls the barotropic decay by affecting the details of $[u]$.

We have focused on low-level barotropic processes and the LLJ because the waves break first at low levels, where eddy fluxes are initially stronger. If the character of the equilibration at upper levels is also ultimately determined by momentum fluxes, as we believe, there is nevertheless an important, indirect role for the vertical wave activity transfer emphasized by THM, especially during and immediately following low-level breaking. Because of the ''invertibility'' of the surface tempera-

ture and low-level PV anomalies in a balanced disturbance, the symmetry and strength of the low-level vortices is projected into upper levels. If the LC2 vortices avoid barotropic decay by becoming and remaining axisymmetric, this influence from low levels may be crucial for establishing the deep, equivalent-barotropic structures discovered by THM. The symmetry of low-level vortices is not directly revealed by zonal-mean EP diagrams.

The CM cyclones decay faster than those in LC2, which seem to weaken only through diffusion. The artificially modified LC2 experiments in which only one zonal wave was retained (the wave–mean-flow version) also showed faster decay. There is obviously much about the long-term coherence of isentropic, equivalent-barotropic vortices that remains unclear. We have noticed in comparing PV maps like those in Fig. 8 that the CM vortices are never able to completely pinch off from their high-PV reservoir and symmetrize in the same way as the vortices in LC2. It is possible that an alignment of PV and streamfunction contours is more difficult in Cartesian geometry. Based on the wave–mean flow experiment, we also speculate that symmetrization can be inhibited by the failure to properly resolve vorticity filaments. We are currently investigating the equilibration of short waves and finding that cyclonic roll-up on the sphere is not as unusual as might appear from longwave studies. However, the fraction of eddy energy that survives in this form is extraordinarily large in cyclonic long waves (LC2). This will be an issue for a future paper on shortwave equilibration.

Though we have found that normal-mode eddy momentum fluxes strongly influence the nonlinear evolution of baroclinic waves, these results are of course limited by the restrictive initial conditions and basic states. Chang and Orlanski (1993) argue that the decay of longitudinally localized eddies is due to downstream dispersion of EKE in wave packets, rather than to the alteration of the mean flow. The observation of poleward momentum fluxes in the earth's atmosphere (Starr 1968; Peixoto and Oort 1984) suggests that the present results might be somewhat more general than modal baroclinic development in zonally symmetric flows. This will need to be confirmed through GCM studies. The recent one by Lee and Feldstein (1996) shows a strong component of variability between cyclonic and anticylonic breaking in wave packets and storm tracks.

We have also ignored moisture, topography, and surface fluxes. James and Gray (1986) found that eddy activity in the statistically steady state is greater when surface friction is included, demonstrating the operation of the barotropic governor. If, as we have suggested, the inviscid equilibration depends crucially on low-level barotropic processes, this result is not surprising, but it implies that normal-mode wave equilibration could be substantially altered by surface drag.

Acknowledgments. The authors thank Drs. I. Orlanski and I. Held for their interest in this study and the valuable discussions we had with them during the progress of the work. The comments and suggestions of Drs. B. Gross, C. D. Thorncroft, C. Snyder, and two anonymous reviewers led to substantial improvement of the original manuscript.

REFERENCES

Andrews, D. G., J. R. Holton, and C. B. Leovy, 1987: *Middle Atmosphere Dynamics.* Academic Press, 489 pp.

Balasubramanian, G., and M. K. Yau, 1994: The effects of convection on a simulated marine cyclone. *J. Atmos. Sci.*, **51,** 2397–2417.

Bourke, W., 1974: A multilevel spectral model. Part I: Formulation and hemispheric integrations. *Mon. Wea. Rev.*, **102,** 687–701.

Branstator, G., 1995: Organization of storm track anomalies by recurring low-frequency circulation anomalies. *J. Atmos. Sci.*, **52,** 207–226.

Chang, K. M., and I. Orlanski, 1993: On the dynamics of a storm track. *J. Atmos. Sci.*, **50,** 999–1015.

Davies, H. C., C. H. Schar, and H. Wernli, 1991: The palette of fronts and cyclones within a baroclinic wave development. *J. Atmos. Sci.*, **48,** 1666–1689.

Edmon, H. J., B. J. Hoskins, and M. E. McIntyre, 1980: Eliassen–Palm cross sections for the troposphere. *J. Atmos. Sci.*, **37,** 2600–2616.

Farrell, B. F., 1989: Optimal excitation of baroclinic waves. *J. Atmos. Sci.*, **46,** 1193–1206.

Feldstein, S. B., and I. M. Held, 1989: Barotropic decay of baroclinic waves in a two-layer beta plane model. *J. Atmos. Sci.*, **46,** 3416–3430.

Gill, A. E., 1982: *Atmosphere–Ocean Dynamics.* Academic Press, 662 pp.

Held, I. M., and D. G. Andrews, 1983: On the direction of the eddy momentum flux in baroclinic instability. *J. Atmos. Sci.*, **40,** 2220–2231.

——, and M. J. Suarez, 1994: A proposal for the intercomparison of the dynamical cores of atmospheric general circulation models. *Bull. Amer. Meteor. Soc.*, **75,** 1825–1835.

Hines, K. M., and R. Mechoso, 1993: Influence of surface drag on the evolution of fronts. *Mon. Wea. Rev.*, **121,** 1152–1175.

Hollingsworth, A., A. J. Simmons, and B. J. Hoskins, 1976: The effect of spherical geometry on momentum transports in simple baroclinic flows. *Quart. J. Roy. Meteor. Soc.*, **102,** 901–911.

Hoskins, B. J., and A. J. Simmons, 1975: A multi-layer spectral model and the semi-implicit method. *Quart. J. Roy. Meteor. Soc.*, **101,** 637–655.

James, I. N., 1987: Suppression of baroclinic instability in horizontally sheared flows. *J. Atmos. Sci.*, **44,** 3710–3720.

——, and L. J. Gray, 1986: Concerning the effect of surface drag on the circulation of a baroclinic planetary atmosphere. *Quart. J. Roy. Meteor. Soc.*, **112,** 1231–1250.

Lee, S., and S. B. Feldstein, 1996: Two types of wave breaking in an aquaplanet GCM. *J. Atmos. Sci.*, **53,** 842–856.

Lorenz, E. N., 1955: Available potential energy and the maintenance of the general circulation. *Tellus*, **7,** 157–167.

McIntyre, M. E., 1970: On the non-separable baroclinic parallel-flow instability problem. *J. Fluid Mech.*, **40,** 273–306.

Mudrick, S., 1974: A numerical study of frontogenesis. *J. Atmos. Sci.*, **31,** 869–892.

Nakamura, N., 1993: Momentum flux, flow symmetry, and the nonlinear barotropic governor. *J. Atmos. Sci.*, **50,** 2159–2179.

Peixoto, J. P., and A. H. Oort, 1984: Physics of climate. *Rev. Mod. Phys.*, **56,** 365–429.

Polavarapu, S. M., and W. R. Peltier, 1990: The structure and nonlinear evolution of synoptic scale cyclones: Life cycle simulations with a cloud-scale model. *J. Atmos. Sci.*, **47,** 2645–2672.

Robert, A. F., 1966: The integration of a low order spectral form of

the primitive meteorological equations. *J. Meteor. Soc. Japan*, **44,** 237–245.

Rotunno, R., W. C. Skamarock, and C. Snyder, 1994: An analysis of frontogenesis in numerical simulation of baroclinic waves. *J. Atmos. Sci.,* **51,** 3373–3398.

Shapiro, M. A., and D. Keyser, 1990: Fronts, jet streams, and the tropopause. *Extratropical Cyclones: The Erik H. Palmen Memorial Volume,* C. W. Newton and E. O. Holopainen, Eds., Amer. Meteor. Soc., 262 pp.

Simmons, A. J., and B. J. Hoskins, 1976: Baroclinic instability on the sphere: Normal modes of the primitive and quasi-geostrophic equations. *J. Atmos. Sci.,* **33,** 1454–1477.

——, and ——, 1977: Baroclinic instability on the sphere: Solutions with a more realistic tropopause. *J. Atmos. Sci.,* **34,** 581–588.

——, and ——, 1978: The life cycles of some nonlinear baroclinic waves. *J. Atmos. Sci.,* **35,** 414–432.

——, and ——, 1980: Barotropic influences on the growth and decay of nonlinear baroclinic waves. *J. Atmos. Sci.,* **37,** 1679–1684.

Snyder, C., W. C. Skamarock, and R. Rotunno, 1991: A comparison of primitive-equation and semigeostrophic simulations of baroclinic waves. *J. Atmos. Sci.,* **48,** 2179–2194.

Starr, V. P., 1968: *Physics of Negative Viscosity Phenomena*. McGraw-Hill, 256 pp.

Takayabu, I., 1986: Roles of the horizontal advection on the formation of surface fronts on the occlusion of a cyclone developing in a baroclinic westerly jet. *J. Meteor. Soc. Japan,* **64,** 329–345.

Thorncroft, C. D., B. J. Hoskins, and M. E. McIntyre, 1993: Two paradigms of baroclinic wave life-cycle behavior. *Quart. J. Roy. Meteor. Soc.,* **119,** 17–55.

Whitaker, J. S., and C. Snyder, 1993: The effects of spherical geometry on the evolution of baroclinic waves. *J. Atmos. Sci.,* **50,** 597–612.

——, and R. M. Dole, 1995: Organization of storm tracks in zonally varying flows. *J. Atmos. Sci.,* **52,** 1178–1191.